Received: Added at production | Revised: Added at production | Accepted: Added at production

DOI: xxx/xxxx

ARTICLE TYPE

A well-balanced positivity-preserving central-upwind scheme for one-dimensional blood flow models†

Gerardo Hernandez-Duenas* | Guillermo Ramirez-Santiago

[1]Institute of Mathematics, National University of Mexico, Blvd. Juriquilla 3001, Querétaro, 76230, México

Correspondence
*Gerardo Hernandez-Duenas, Institute of Mathematics, National University of Mexico, 76230. Email: hernandez@im.unam.mx

Present Address
Blvd. Juriquilla 3001, Querétaro, México, 76230

Summary

In this work, we consider a hyperbolic one-dimensional (1D) model for blood flow through compliant axi-symmetric tilted vessels. The pressure is a function of the cross-sectional area and other model parameters. Important features of the model are inherited at the discrete level by the numerical scheme. For instance, the existence of steady states may provide important information about the flow properties at low computational cost. Here, we characterize a large class of smooth equilibrium solutions by means of quantities that remain invariant. At the discrete level, the well-balanced property in the numerical scheme leads to accurate results when steady states are perturbed. On the other hand, the model is equipped with an entropy function and an entropy inequality that can help us choose the physically relevant weak solutions. A large class of semi-discrete entropy-satisfying numerical schemes is described. In addition, preservation of positivity for the cross-sectional area is achieved. Numerical results show the scheme is robust, stable and accurate. The ultimate goal of this paper is the numerical application to cases that are more relevant from the medical point of view. In particular, a numerical simulation of cardiac cycles with appropriate parameters shows that increasing the rigidity of the artery walls delays the formation of shock waves. Gravity effects are also measured in tilted vessels, and a simulation using an idealized aorta model was conducted.

KEYWORDS:
Blood flows, Hyperbolic balance laws, Central-upwind schemes

1 | INTRODUCTION

The increasing impact of cardiovascular diseases in our lives is a driving motivation to propose and investigate a variety of mathematical models of blood flow [1,2,3,4,5,6,7,8,9,10,11,12]. Detailed numerical simulations of blood flows in conjunction with laboratory investigations are very helpful in the diagnosis and treatment of cardiovascular diseases. Three-dimensional (3D) models can accurately provide most of the details of the local blood flow distribution, flow recirculation, local flow patterns, and wall shear stresses. However, 3D simulations are computationally expensive and are not always practical to obtain a rapid evaluation of surgical treatments. As an alternative to complex 3D models, one can use 1D models, which are simpler and cheaper, and require less computational resources [13,14,15,16]. It has been shown that 1D models reasonably well describe the propagation of pressure waves in arteries [16] as well as the effects of variations of the mechanical properties of arteries due to stenosis or aneurysms on

†Research supported in part by grants Conacyt A1-S-17634 (GHD), UNAM-DGAPA-PAPIIT IN113019 (GHD) & IN108916 (GRS) (Investigación realizada gracias a los programas Conacyt A1-S-17634 (GHD), UNAM-DGAPA-PAPIIT IN113019 (GHD) & IN108916 (GRS))

pulse waves [17,18,19]. In [20], it was noted that 1D models are able to describe the fluid's evolution after arteriovenous fistula (AVF) surgeries, and experimental validations showed that flow can be predicted in 6/10 patients. A good agreement between 1D and 3D models was also reported in [13] for pulsatile blood flows in patient-specific intracranial arterial networks. In [21], another comparison between 1D and 3D models for blood flow passing through the aorta showed very good agreement when the model parameters are carefully chosen.

Most existing 1D models are based on conservation of fluid mass and momentum together with an equation of state that relates the vessel cross-sectional area with the associated pressure. As a result, a hyperbolic system of partial differential equations is obtained [22,15,4]. In [10], well-balanced, high-resolution numerical schemes were constructed for 1D blood flows in elastic vessels with different mechanical properties. The well-balanced property was obtained using the so-called generalized hydrostatic reconstruction. This technique was first introduced in [23] to obtain a numerical scheme that is well balanced for a predetermined family of stationary solutions in the context of path-conservative schemes. A 1D model was proposed in [4] to study blood flows through compliant axi-symmetric vessels, i.e., vessels that distend and increase volume with increasing transmural pressure. Despite its simplicity, the model provided useful information about blood flow dynamics. For instance, it was found that vessel tapering postpones shock formation [4]. In [11], a more elaborated 1D model for blood flows in vessels with walls having viscoelastic properties was analyzed. In this case, the advection-diffusion-reaction problem was reformulated by applying a relaxation technique to obtain a hyperbolic system with stiff source terms in the context of well-balanced and non-conservative schemes. A high order non-linear numerical scheme for 1D blood flow models was implemented in [24].

Hyperbolic balance laws have been extensively studied, and a variety of numerical schemes have been developed (e.g., see [25,26]). Central/central-upwind numerical schemes in [27,28] use a semi-discrete formulation with the aid of numerical fluxes, and such schemes were further developed in [29,30,31]. Central schemes are based on the viscous form of the Lax-Friedrichs scheme, with a possible generalization involving replacing the first-order piecewise constant solution with a MUSCL-type piecewise linear reconstruction to achieve second-order accuracy in smooth regions [27]. On the other hand, central-upwind schemes have more precise one-sided local speeds of propagation in the computation of numerical fluxes. In particular, the local speeds take into account the sign of the eigenvalues, similar to the upwind-type schemes. See [28] for more details. This reduces the numerical dissipation while maintaining the simplicity of the central-upwind schemes. Central-upwind schemes are free of Riemann solvers, which represents an advantage when the eigenvalues of the associated Jacobian have no explicit analytic expressions. See [32,33] and references therein.

In the present paper, we conduct a theoretical analysis of the hyperbolic properties of a 1D model for blood flow through compliant axi-symmetric tilted vessels. The pressure is an increasing function of the vessel cross-sectional area and viceversa. It may also depend on other parameters, such as the unstressed cross-sectional area and given elasticity parameters. The hyperbolic model is written in balanced form. The source terms do not involve non-conservative products, which avoids both theoretical and numerical complications. The numerical scheme we propose inherits many other important properties of the model at a discrete level, adding robustness and accuracy to the numerical approximations. For instance, the model is equipped with an entropy inequality that can be used to determine the physically relevant weak solutions. At the discrete level, entropy-satisfying semi-discrete schemes may be constructed. Steady states are by definition those that are time independent, and a large class of such equilibrium states can be characterized by invariants in this model. In specific situations, they can provide relevant information at lower computational cost. In [34] it was shown that steady states were particularly helpful in the analysis of intracranial aneurysms. We show that the numerical scheme satisfies the well-balanced property, adding accuracy near steady states.

The analysis of the theoretical features of the model and the presentation of a robust and accurate numerical scheme are important components of the paper. Numerical tests show that the numerical scheme is stable, robust and accurate. The ultimate goal of this paper is the numerical application in cases that are more relevant from the medical point of view. Consequently, the model is applied to some of those possible relevant situations. In particular, the effect of different heterogeneous elastic properties in the formation of shock waves is analyzed in both horizontal and tilted vessels. Ignoring bifurcations and approximating the geometry of the aorta, numerical simulations under appropriate model parameters show a reasonable qualitative approximation of other observations and results available in the literature using 1D and 3D models. From the medical point of view, the above applications represent one of the main contributions of this work.

The remainder of this paper is organized as follows. The properties of the model are discussed in Section 2. Solutions to the Riemann problem are also constructed in this section. Furthermore, we show that the model admits an entropy function and an entropy inequality in the inviscid case. The details of the semi-discrete central-upwind scheme are presented in Section 3. In this section, we also prove the well-balanced and positivity-preserving properties. A large class of entropy-satisfying semi-discrete numerical schemes is also described. Section 4 encompasses a variety of numerical tests that demonstrate the merits

of the numerical scheme. The model is applied to other relevant situations, including a cardiac cycle in tilted vessels and blood flow simulations in the aorta. The conclusions are left in Section 5, where we discuss the main contributions of the paper, the limitations of the current approach, and possible implications of this work.

2 | PROPOSED MODEL AND ITS PROPERTIES

There are four basic components that comprise human blood: plasma, red blood cells, white blood cells, and platelets. Red blood cells become significant in regions with small volume fraction with diameters $< 200\ \mu m$[35]. As a result, blood flow is non-Newtonian in arterioles or capillaries. However, in long vessels, blood behaves as an incompressible and Newtonian fluid[36,13]. Taking this into consideration, here we analyze blood flow through long axi-symmetric vessels.

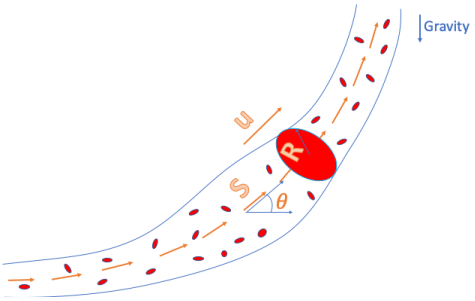

FIGURE 1 Sketch of blood flow passing through a compliant axi-symmetric vessel. The two variables to compute in this model are the cross-sectional area A and discharge Au.

We consider a cylindrical vessel with variable cross-sectional area $A(s,t) = \pi R(s,t)^2$ and velocity $u(s,t)$ at time t and arc length position s. Here, $R(s,t)$ is the cross-sectional radius. The upstream boundary corresponds to $s = 0$. For horizontal vessels, we will replace the arc length position with the x coordinate. We assume that at a given position s, the vessel forms an angle $\theta(s)$ with respect to the horizontal axis, and we take into account the gravity effect in tilted or vertical vessels. See[37] for more details. A schematic diagram of the model is shown in Figure 1.

The elastic properties of the vessel wall can be described by the relation between pressure and cross-secional area. However, such relationship is not solely mechanical; it can be affected by contraction of surroundings muscles, physiological features (auto-regulation), pathologies (aneurysms), and other conditions[37]. On the other hand, the overall vessel's elastic properties are mainly determined by the internal radius and wall thickness. One parameterization of the pressure is provided below. In this work, we consider a general case of a transmural pressure $p = p(A, s)$, which is a monotone function of the cross-sectional area that may also depend on other model parameters, which in turn are explicit functions of arc length position. This relationship between the pressure and the other variables describes the vessel's deformability. The arc length position's explicit dependence will be used to model the blood flow in a vessel with non-uniform elastic properties. The following notation will be used for the partial derivatives of $p(A, s)$ with respect to A and s, respectively:

$$\partial_1 p = \frac{\partial p(A,s)}{\partial A}, \qquad \partial_2 p = \frac{\partial p(A,s)}{\partial s},$$

which means we can write

$$\partial_s \left(p(A(s,t),s)\right) = \partial_1 p\ \partial_s A + \partial_2 p.$$

We note that $\partial_2 p$ is a spatial derivative calculated for a fixed value of A. We will assume that the transmural pressure vanishes at an unstressed cross-sectional area $A_o(s)$ for horizontal arteries, i.e., $p(A_o(s), s) = 0$. For hyperbolicity the following condition is required:

$$\partial_1 p(A,s) > 0 \quad \text{for any} \quad A > 0.$$

The model described below was derived in[4] by cross-averaging the Navier-Stokes equations in cylindrical coordinates and focusing on a particular expression for the pressure. Here, we also include gravity effects for non-horizontal vessels. In the

derivation of the model, the walls were assumed to be streamlined. It is assumed that the vessel's length scale L is much larger than its radial extension R_o. Because of this, the ratio $\epsilon = R_o/L$ is a small parameter that can be used to write asymptotic expansions.

The resulting system of PDEs is based on mass and momentum balance, and a primary version of model is written as

$$\begin{aligned} A_t + (Au)_s &= 0, \\ (Au)_t + (\alpha Au^2)_s + \tfrac{A}{\rho}\partial_s p_{\text{int}} &= -2\pi \tfrac{\alpha\nu}{\alpha-1} u - gA\sin(\theta(s)), \end{aligned}$$

where u is blood velocity, p_{int} is internal pressure, ρ is constant density, ν is viscosity, α is the Coriolis velocity-distribution coefficient as will be described below, g is the acceleration of gravity, and $\theta(s)$ is the vessel's angle with respect to the horizontal axis at arc length position s. See[4] for a detailed derivation of the friction term with coefficient ν. Furthermore, we assume that the internal pressure is decomposed as $p_{\text{int}} = p_{\text{ext}} + p$, where p_{ext} and p are the external and transmural pressures, respectively. For simplicity, we also assume that the external pressure is constant and does not appear in the pressure gradient. The term associated with the pressure gradient can be decomposed as the sum of a gradient plus a source term:

$$\begin{aligned} \tfrac{A}{\rho} p_s &= \tfrac{A}{\rho}\partial_1 p(A,s)\partial_s A + \tfrac{A}{\rho}\partial_2 p = \partial_s\left(\int_{A_o(s)}^{A} \tfrac{\mathcal{A}}{\rho}\partial_1 p(\mathcal{A},s)d\mathcal{A}\right) - \partial_2\left(\int_{A_o(s)}^{A} \tfrac{\mathcal{A}}{\rho}\partial_1 p(\mathcal{A},s)d\mathcal{A}\right) + \tfrac{A}{\rho}\partial_2 p \\ &= \partial_s\left(\tfrac{1}{\rho}A\hat{p}\right) + \tfrac{1}{\rho}A\partial_2\bar{p}, \end{aligned}$$

where

$$\bar{p}(A,s) = \frac{1}{A}\int_{A_o(s)}^{A} p(\mathcal{A},s)d\mathcal{A}, \qquad \text{and} \qquad \hat{p}(A,s) = p(A,s) - \bar{p}(A,s).$$

The decomposition $p = \bar{p} + \hat{p}$ does not have an explicit physical significance and it is different compared to the usual decomposition done in other systems such as in the 1-D mathematical modelling of shallow water open-channel flows. The shallow water equations can be derived by cross-sectional averaging of the Euler equations, assuming a hydrostatic pressure. The integration of the pressure gradient is decomposed into conservative and source terms. In the derivation of the above model for blood flows, a scaling analysis gives a pressure that is independent in the radial direction before the pressure gradient is integrated in each cross section. The equivalent decomposition into conservative and source terms need the unusual decomposition described in the previous equation.

Note that we are using the symbol $\mathcal{A}$ as an integration variable. By integrating by parts and using the condition $p(A_o(s), s) = 0$, the following relation is obtained:

$$\hat{p}(A,s) = \frac{1}{A}\int_{A_o(s)}^{A(s,t)} \mathcal{A}\partial_1 p(\mathcal{A},s)d\mathcal{A}.$$

The "correction" term $\alpha \geq 1$ takes into account the non-uniform distribution of the velocity in each cross section and is given by

$$\alpha = \frac{\overline{U^2}}{\bar{U}^2},$$

where U is the velocity in the 3D Navier-Stokes equations, and $\overline{(\cdot)}$ denotes the cross-sectional average. For simplicity, α is assumed constant.

Regarding the viscosity term, a scaling analysis of the Navier-Stokes equations in cylindrical coordinates[4] in the present setting shows that the radial component of the Laplacian is the leading contribution. When the Navier-Stokes equations are integrated in each cross-section, the contribution of the viscosity term in the radial direction reduces to

$$2\nu\pi R\left[\frac{\partial U}{\partial r}\right]_{r=R},$$

where r is the radius in cylindrical coordinates when solving the Navier-Stokes equations. The velocity profile

$$U = \frac{\gamma+2}{\gamma}u\left[1 - \left(\frac{r}{R}\right)^{\gamma}\right]$$

is assumed such that $\overline{U} = u$ and γ is related to α by $\gamma = (2-\alpha)/(\alpha-1)$. This is a Hagen-Poiseuille profile. Physically, this profile vanishes at the walls and reaches its maximum at the artery's center. The exponent α controls the transition from the wall

to the center. We note that $\gamma \to \infty$ and $U \to u$ as $\alpha \to 1$. Substituting the above relations in the momentum equations results in the viscosity term. See section 2.4 in[4] for further discussion. We always take $\nu = 0$ when $\alpha = 1$. The above term reduces to

$$2\nu\pi R\left[\frac{\partial U}{\partial r}\right]_{r=R} = -2\pi\frac{\alpha\nu u}{\alpha-1}.$$

We note that $\gamma = 2$ corresponds to the classic Hagen-Poiseuille profile. In this case $\alpha = 4/3$, and the above term reduces to $-8\pi\nu u$.

The model written in conservation/balanced form for blood flow in compliant axi-symmetric vessels with constant density and pressure $p = p(A, s)$ is given by

$$\begin{aligned} \partial_t A \quad &+ \partial_s(Au) &&= 0 \\ \partial_t(Au) &+ \partial_s\left(\alpha Au^2 + \tfrac{1}{\rho}A\hat{p}(A,s)\right) &&= -2\pi\tfrac{\alpha\nu u}{\alpha-1} - \tfrac{1}{\rho}A\partial_2\bar{p}(A,s) - gA\sin(\theta(s)). \end{aligned} \tag{1}$$

Equation (1) forms a hyperbolic system of balance laws, as will be described below. The source terms have no derivates of the solution (unknown) but only derivatives of the model's parameters. This is an important distinction because source terms of this type do not alter the Rankine-Hugoniot conditions. This avoids both theoretical and numerical complications. A model for multi-phase blood flows is derived in[38], which involves non-conservative products. In that setting, weak solutions may be defined based on the theory of non-conservative products[39]. The theory of paths found in[40,41] can be used to construct solutions to the Riemann problem. Possible computational issues are analyzed in[42].

Special case:

As discussed above, the elastic properties of the vessel can be described by assuming that the pressure depends on the cross-sectional area A. Physical experiments[37] show that p must be a monotonic function of A, which is also required for hyperbolicity. Although deriving an explicit dependence $p = p(A, s)$ is complicated, valid expressions for arteries and collapsible tubes such as veins can be found in[10]. Other approaches are presented in[37]. The numerical tests in the present paper are conducted using the transmural pressure introduced in[4], which includes the effect of the wall's thickness and the stress-strain response on the elastic properties of the vessel. The pressure is given by

$$p(A, s) = G_o(s)\left[\left(\frac{A}{A_o(s)}\right)^{\beta/2} - 1\right], \tag{2}$$

where $A_o = A_o(s)$ is an unstressed cross-sectional area for horizontal arteries, and $G_o = G_o(s)$ is the elasticity parameter proportional to Young's modulus. Shear stress is ignored, and is assumed that the pressure of blood is the only force exerted on the vessel walls. The exponent β is the stress-strain response parameter and it is assumed to be constant. Adopting the parameterizations of G_o in terms of Young's modulus and wall thickness in[21], we get

$$G_o(s) = \frac{4}{3}E_Y\frac{h_d}{r_d}, E_Y = \frac{3}{2}\rho\frac{r_d}{h_d}c_d^2, \tag{3}$$

where E_Y is Young's modulus, r_d is the radius at diastolic pressure, h_d is the wall's thickness, and c_d is the pulse wave speed.

As mentioned above, other parameterization exist for collapsible tubes, such as veins and arteries, involving different powers of the fraction A/A_o[10]. The expression associated to arteries coincides with the choice above.

System (1) then becomes

$$\begin{aligned} \partial_t A \quad &+ \partial_s(Au) &&= 0 \\ \partial_t(Au) &+ \partial_s\left\{\alpha Au^2 + \tfrac{G_o\beta A_o}{\rho(\beta+2)}\left[\left(\tfrac{A}{A_o}\right)^{\frac{\beta+2}{2}} - 1\right]\right\} &&= -2\pi\tfrac{\alpha\nu u}{\alpha-1} + \left[\left(\tfrac{A}{A_o}\right)^{\frac{\beta+2}{2}} - 1\right]\tfrac{d}{ds}\left(\tfrac{G_oA_o\beta}{\rho(\beta+2)}\right) \\ & && \quad -\tfrac{AG_o'(s)}{\rho}\left[\left(\tfrac{A}{A_o}\right)^{\frac{\beta}{2}} - 1\right] - gA\sin(\theta(s)). \end{aligned} \tag{4}$$

2.1 | Quasi-linear formulation of the model

The hyperbolic properties of system (1) can be analyzed using the quasi-linear form described in the following proposition.

Proposition 1. System (1) can be written in quasi-linear form as

$$\partial_t\begin{pmatrix} A \\ Au \end{pmatrix} + \begin{pmatrix} 0 & 1 \\ c^2 - \alpha u^2 & 2\alpha u \end{pmatrix}\begin{pmatrix} A \\ Au \end{pmatrix}_s = \begin{pmatrix} 0 \\ -2\pi\frac{\alpha\nu}{\alpha-1}u - \frac{A}{\rho}\partial_2 p(A,s) - gA\sin(\theta(s)) \end{pmatrix}, \tag{5}$$

where

$$c = \sqrt{\frac{A\partial_1 p}{\rho}}$$

is the equivalent to the speed of sound in gas dynamics. The eigenvalues and corresponding eigenvectors are

$$\lambda_1 = \alpha u - \sqrt{\alpha(\alpha-1)u^2 + c^2}, \quad \lambda_2 = \alpha u + \sqrt{\alpha(\alpha-1)u^2 + c^2}, \quad \mathbf{r}_1 = \begin{pmatrix} 1 \\ \lambda_1 \end{pmatrix}, \text{ and } \mathbf{r}_2 = \begin{pmatrix} 1 \\ \lambda_2 \end{pmatrix},$$

respectively.

We note that the quantities $\bar{p}$ and $\hat{p}$ do not appear in the quasilinear form. In fact, the quasilinear form is easily derived from the primary version of the model. The proof uses standard arguments and is omitted here. The characteristic polynomial is $p(\lambda) = \lambda^2 - 2\alpha u\lambda + \alpha u^2 - c^2$. We note that the eigenvalues are always real, and the eigenvectors form a basis unless $A = 0$ and either $u = 0$ or $\alpha = 1$. This is because $\partial_1 p$ is positive for $A > 0$ and it may vanish only when $A = 0$. Therefore, hyperbolicity is lost only when the vessel collapses. The eigenvalues and eigenvectors have explicit analytic expressions, which is an advantage when implementing numerical schemes based on approximate Riemann solvers, such as Roe-type upwind schemes.

2.2 | Steady states

Computational hemodynamics simulations can provide important information about patients with intracranial aneurysms. Transient simulations can accurately describe pulsatile blood flows. However, in[34], it is shown that under certain circumstances, steady-state simulations might provide enough information for clinical assessment at lower computational cost. For instance, in the above reference, a 5% difference was found between transient and steady states. The variable utilized in this measure was the time-averaged wall shear stress. Although the results provide qualitatively accurate hemodynamic information in specific cases, there are other clinical situations where it is necessary to consider the description of transient flows. The present paper focuses on the description of a numerical scheme that can accurately compute near steady states, improving the results obtained in simulations involving convergence to steady states. In the following proposition, smooth equilibrium solutions are characterized, including the case of positive viscosity, by providing, either invariants or ODEs for the most general case.

Proposition 2. Smooth steady-state solutions of system (1) are given by the following conditions

$$Q = Au = \text{const.}, \qquad \partial_s E = -2\pi \frac{\alpha\nu}{\alpha - 1}\frac{Q}{A^2}, \tag{6}$$

where Q is the discharge, $E = \frac{\alpha}{2}u^2 + \frac{p}{\rho} + gz$ is the energy of the system, $z = \int_{s_o}^{s} \sin(\theta(s))ds$ is the elevation above a reference height, and $s_o = 0$ corresponds to the left end of the vessel. In particular, the energy remains constant when $\nu = 0$.

The proof uses standard arguments and is omitted.

Note: For smooth steady state flows with $\nu > 0$, the energy is a decreasing/increasing function of s when the velocity is positive/negative. As a result, the energy decreases in the direction of the fluid's motion. Discontinuous steady state solutions may arise when the left and right boundary conditions are not connected by a smooth state. In that case, the solution must jump to match both boundary conditions. The jump in the solution occurs in the place where the Rankine-Hugoniot conditions are satisfied. On the contrary, discontinuous steady state solutions have a piecewise constant energy and a constant discharge when $\nu = 0$.

Steady states at rest satisfy the following static conditions:

$$u = 0, P = p(A, s) + g\rho z(s) = \text{const.} \tag{7}$$

Because $p(A_o(s), s) = 0$, a particular steady state at rest for horizontal arteries ($\theta = 0$) is given by

$$u = 0, A = A_o(s). \tag{8}$$

We call A_o an unstressed cross-sectional area because the transmural pressure vanishes at $A = A_o$. However, we can see from equation (7) that this is not the only one. We construct the well-balanced property in the special case given by equation (8).

When the viscosity ν is positive, the steady states described in Proposition 2 are given by an ODE in the s variable. In the special case when the model parameters are independent of s, one can obtain another invariant as stated in the following corollary.

Corollary 1. Let us assume $\nu > 0$ and $\theta = 0$. If the unstressed cross-sectional A_o is constant and the pressure is an explicit function of cross-sectional area A ($p = p(A)$), then smooth steady states satisfy

$$Q = \text{Const.}\ ,\ \alpha Q^2 \ln\left(\frac{A}{A_o}\right) - I - 2\pi\frac{\alpha}{\alpha-1}\nu Q\ s = \text{Const.}, \tag{9}$$

where I is defined as

$$I = \int_{A_o}^{A} \frac{\mathcal{A}^2}{\rho}\partial_1 p(\mathcal{A}) d\mathcal{A}.$$

Proof. By equation (6), substituting $Au_s = -uA_s$ for the steady state, and $u = Q/A$, we get

$$\alpha Q^2 \frac{1}{A/A_o}\partial_s\left(A/A_o\right) - \frac{A^2}{\rho}\partial_1 p(A)\partial_s A = 2\pi\frac{\alpha}{\alpha-1}\nu Q.$$

The conclusion of the proof follows after integration with respect to s and using the fact that Q is constant. □

To the best of our knowledge, this is the first time that the invariant quantity expressed in equation (9) has been reported. This invariant has no direct physical significance and it is just an antiderivative of $-A^2\partial_s E - 2\pi\alpha\nu/(\alpha-1)Q$. However, this invariant determines the effect of viscosity in such steady states.

For the special case when the pressure is given by (2) and G_o and A_o are constants, the quantity I is given by

$$I = \frac{G_o}{\rho}\frac{\beta}{\beta+4}A_o^2\left[\left(\frac{A}{A_o}\right)^{\beta/2+2} - 1\right].$$

2.3 | Solution to the Riemann problem

Exact solutions to system (1) are not available in general, especially for discontinuous initial conditions. An exception is the Riemann problem when $\theta = 0$, $\nu = 0$ and $\alpha = 1$ and the model parameters, including A_o, are fixed such that $p = p(A)$ is only a function of A. The initial conditions are given by

$$A(s,0) = \begin{cases} A_\ell & \text{if}\ \ s \le 0 \\ \\ A_r & \text{otherwise,} \end{cases}, \quad Q(s,0) = \begin{cases} Q_\ell & \text{if}\ \ s \le 0 \\ \\ Q_r & \text{otherwise,} \end{cases}$$

where (A_ℓ, Q_ℓ) and (A_r, Q_r) are the constant left and right states, respectively. The corresponding solution consists of two wave families, each of them associated to an eigenvalue λ_1 or λ_2. The two waves are genuinely non-linear and can be either a shock wave (discontinuous jump) or a rarefaction wave (smooth function of $\xi = s/t$).

We note that the Riemann problem has no direct physical significance in hemodynamics. However, one can use the exact solutions to verify the accuracy of the proposed scheme. Numerical tests below will show that our numerical scheme is second-order accurate in smooth regions and it becomes first-order accurate near discontinuities.

Rarefaction waves and Riemann invariants for $p = p(A)$:

The first and/or second rarefaction wave families have the following Riemann invariants:

$$u + C, u - C,$$

where $C = \int_0^A \frac{c(\mathcal{A})}{\mathcal{A}} d\mathcal{A}$. These quantities remain constant across such waves, which together with the relation $\lambda_{1,2} = \xi = s/t$, leads to rarefaction wave solutions in the first or second family.

Special case for pressure given by equation (2):

For the special case of pressure given by equation (2) and assuming that (A_ℓ, Q_ℓ) and (A_r, Q_r) are connected by a rarefaction wave, we have $C = \frac{4}{\beta}c$, $c = \sqrt{\frac{G_o}{\rho}\frac{\beta}{2}\left(\frac{A}{A_o}\right)^{\beta/2}}$, and

$$A(s,t) = \begin{cases} A_\ell & \text{if } \ s/t \le \lambda_p^\ell, \\ A_0\left[\frac{2\beta\rho}{G_0(\beta+4)^2}\left(u_r \pm \frac{4}{\beta}c_r - \frac{s}{t}\right)^2\right]^{2/\beta} & \text{if } \ \lambda_p^\ell \le s/t \le \lambda_p^r, \\ A_r & \text{if } \ s/t \ge \lambda_p^r, \end{cases}$$

$$u(s,t) = \begin{cases} u_\ell & \text{if } \ s/t \le \lambda_p^\ell, \\ \left(\frac{4}{\beta+4}\right)\frac{s}{t} + \left(\frac{\beta}{\beta+4}\right)\left(u_r \pm \frac{4}{\beta}c_r\right) & \text{if } \ \lambda_p^l \le s/t \le \lambda_p^r, \\ u_r & \text{if } \ s/t \ge \lambda_p^r. \end{cases}$$

We note that given any left and right states, the solution to the Riemann problem consists of two elementary waves with a star region connecting the left and right waves. In the case of a left-rarefaction wave, (A_r, Q_r) is replaced by (A^*, Q^*). On the contrary, in the case of a right rarefaction wave, (A_ℓ, Q_ℓ) is replaced by (A^*, Q^*).

Shock waves for $p = p(A)$

When the states (A_ℓ, u_ℓ) and (A_r, u_r) are connected through a shock wave, they satisfy ($\alpha = 1$)

$$\begin{aligned} \Delta(Au) &= \mathfrak{s}\Delta A \\ \Delta\left(\alpha A u^2 + \tfrac{A}{\rho}\hat{p}(A)\right) &= \mathfrak{s}\Delta(Au), \end{aligned}$$

where $\Delta(\cdot) = (\cdot)_r - (\cdot)_\ell$ denotes the difference between left and right states, and $\mathfrak{s}$ is the shock wave speed of propagation. Straightforward calculations yield

$$\Delta u = \mp\frac{\hat{c}}{\sqrt{A_\ell A_r}}\Delta A,$$

where $\hat{c}^2 = \frac{\Delta\left(\frac{A\bar{p}(A)}{\rho}\right)}{\Delta A} > 0$. A_ℓ must be greater/smaller than A_r for the first/second family. In any case, we should have $\lambda_p^\ell > \lambda_p^r$ for any of the families. Furthermore, the speed of the shock wave for the first/second family is given by

$$\mathfrak{s} = \frac{\sqrt{A_\ell}u_\ell + \sqrt{A_r}u_r}{\sqrt{A_\ell} + \sqrt{A_r}} \mp \hat{c}.$$

As explained for the rarefaction case, a left-shock connects (A_ℓ, Q_ℓ) and (A^*, Q^*). In that case, (A_r, Q_r) was replaced by (A^*, Q^*). The opposite occurs for a right-shock, where (A_ℓ, Q_ℓ) is replaced by (A^*, Q^*).

2.4 | Entropy inequalities for $p = p(A, s)$, $\nu = 0$, and $\theta = 0$

System (1) is endowed with an entropy function in the inviscid case ($\nu = 0$), which can help in choosing the correct weak solution [43,44]. The details are given in the following proposition, and similar results have also been proved in [10]. In the next section, we also describe entropy-satisfying semi-discrete numerical schemes and show that a large class of them inherit this property.

Proposition 3. Let us consider the system of PDEs (1) with parameter values $\alpha = 1$, $\nu = 0$ and $\theta = 0$ and general pressure $p(A, s)$ satisfying $\partial_1 p(A, s) > 0$ for all $A > 0$. Then,

$$\mathcal{E} = A\left(\frac{1}{2}u^2 + \frac{1}{\rho}\bar{p}(A, s)\right) \tag{10}$$

is an entropy function of the system that satisfies the entropy inequality

$$\partial_t \mathcal{E} + \partial_s (QE) \le 0. \tag{11}$$

Proof. Adding a friction term $-\epsilon u$ to the momentum equation and rewriting the flux gradient in terms of the discharge $Q = Au$ and the energy $E = \frac{\alpha}{2}u^2 + p/\rho$, we obtain

$$\begin{aligned} A_t + Q_s &= 0 \\ Q_t + \alpha u Q_s + A\partial_s E &= -(\epsilon + 2\pi\tfrac{\alpha\nu}{\alpha-1})u. \end{aligned}$$

Multiplying the momentum equation by the velocity and combining it with the first equation, we obtain

$$\partial_t\left(A\frac{1}{2}u^2\right) = \left(E - \left(\alpha - \frac{1}{2}\right)u^2\right)Q_s - (QE)_s - \left(\epsilon + 2\pi\frac{\alpha\nu}{\alpha-1}\right)u^2. \tag{12}$$

The pressure $p = p(A, s)$ is an explicit function of $A(s, t)$ and s. This gives

$$\partial_t\left(\frac{Ap}{\rho}\right) = -\left(c^2 + \frac{p}{\rho}\right)Q_s. \tag{13}$$

We set $\alpha = 1$ and $\nu = 0$ so that $E - (\alpha - \frac{1}{2})u^2 = \frac{p}{\rho}$. Adding equations (12) and (13), we get

$$\partial_t\left[A\left(\frac{1}{2}u^2 + \frac{p}{\rho}\right)\right] = -c^2Q_s - (QE)_s - \epsilon u^2 = c^2A_t - (QE)_s - \epsilon u^2 = \partial_t\left(\frac{A\hat{p}(A,s)}{\rho}\right) - (QE)_s - \epsilon u^2,$$

which concludes the proof.

□

3 | NUMERICAL SCHEME

In this section, we describe the central-upwind numerical scheme implemented for solving equation (1) and the scheme's properties. In particular, a large class of entropy-satisfying semi-discrete numerical schemes is described. The well-balanced and positivity-preserving properties are also described in this section.

3.1 | Entropy-satisfying semi-discrete schemes for hyperbolic balance laws

Entropy inequalities can help in choosing the correct weak solutions. As shown in Proposition 3, our model has an associated entropy function (10) that satisfies the entropy inequality (11). Satisfying the entropy inequality at a discrete or semi-discrete level is a desirable property of any numerical scheme. For instance, in reference[45], semi-discrete entropy inequalities are proposed, and in reference[46], numerical schemes with that property for the two-layer shallow water equations are used. In this section, we use a similar approach to show the conditions under which a class of numerical schemes satisfies the semi-discrete entropy inequalities.

Let us consider a hyperbolic balance law of the form

$$\mathbf{W}_t + (\mathbf{F}(\mathbf{W}, s))_s = \mathbf{S}(\mathbf{W}, s), \tag{14}$$

where both the flux and source may have terms that depend on the spatial variable s. Some systems may be enabled with an associated entropy function $\mathcal{E}(\mathbf{W}, s)$, an entropy flux $G(\mathbf{W}, s)$ and an entropy inequality

$$\partial_t(\mathcal{E}(\mathbf{W}(s,t), s)) + \partial_s(G(\mathbf{W}(s,t), s)) \leq 0. \tag{15}$$

For smooth flows, we have $\partial_t\mathcal{E} = \frac{\partial\mathcal{E}}{\partial\mathbf{W}}\cdot\mathbf{W}_t = -\frac{\partial\mathcal{E}}{\partial\mathbf{W}}\frac{\partial\mathbf{F}}{\partial\mathbf{W}}\mathbf{W}_s + \frac{\partial\mathcal{E}}{\partial\mathbf{W}}\cdot\mathbf{S}$. We require the entropy function and entropy flux to satisfy

$$\frac{\partial\mathcal{E}}{\partial\mathbf{W}}\frac{\partial\mathbf{F}}{\partial\mathbf{W}} = \frac{\partial G}{\partial\mathbf{W}}, \qquad \frac{\partial\mathcal{E}}{\partial\mathbf{W}}\cdot\mathbf{S} = -\partial_2 G, \tag{16}$$

where it should be recalled that the notation $\partial_2 G(\mathbf{W}, s)$ is the derivative of G with respect to s with $\mathbf{W}$ fixed.

We partition the spatial domain into grid cells $I_j := [s_{j-\frac{1}{2}}, s_{j+\frac{1}{2}}]$, where Δs is the spatial scale, $s_{j\pm\frac{1}{2}} = s_j \pm \frac{\Delta s}{2}$, and s_j is the center of the grid cell. Let us denote by $\overline{\mathbf{W}}_j(t)$ the computed cell average of $\mathbf{W}(s, t)$ over the cell I_j, which is defined as

$$\overline{\mathbf{W}}_j(t) = \frac{1}{\Delta s}\int_{s_{j-\frac{1}{2}}}^{s_{j+\frac{1}{2}}} \mathbf{W}(s,t)\,ds. \tag{17}$$

Furthermore, let us consider a semi-discrete formulation of equation (14) given by

$$\frac{d}{dt}\overline{\mathbf{W}}_j = -\frac{\mathbf{F}_{j+\frac{1}{2}} - \mathbf{F}_{j-\frac{1}{2}}}{\Delta s} + \overline{\mathbf{S}}_j. \tag{18}$$

Following[46], we provide the following definition to be used below.

Definition 1. Consider system (14). We say that an associated semi-discrete numerical scheme is entropy-satisfying if there exists a numerical entropy flux function $G_{j+\frac{1}{2}}$ consistent with $G(\mathbf{U}, s)$ such that

$$G_{j+\frac{1}{2}} - G_{j-\frac{1}{2}} \leq \frac{\partial \mathcal{E}}{\partial \mathbf{W}}(\overline{\mathbf{W}}_j) \cdot \left(\mathbf{F}_{j+\frac{1}{2}} - \mathbf{F}_{j-\frac{1}{2}} - \Delta s \overline{\mathbf{S}}_j\right).$$

3.2 | A class of entropy-satisfying semi-discrete numerical schemes for the blood flow model for $p = p(A)$

Our model (1) has conservative variables and a flux function given by

$$\mathbf{W} = \begin{pmatrix} A \\ Au \end{pmatrix}, \qquad \mathbf{F}(\mathbf{W}, s) = \begin{pmatrix} Au \\ \alpha A u^2 + \frac{A\hat{p}(A,s)}{\rho} \end{pmatrix} \tag{19}$$

on the left hand side, and the source term is given by

$$\mathbf{S} = \begin{pmatrix} 0 \\ -2\pi \frac{\alpha \nu u}{\alpha - 1} - \frac{A\partial_2 \tilde{p}(A,s)}{\rho} - gA\sin(\theta(s)) \end{pmatrix}. \tag{20}$$

We note that for the special case with $\nu = 0, \alpha = 1$, and $\theta = 0$,

$$\frac{\partial \mathcal{E}}{\partial W} = \left(-\tfrac{1}{2}u^2 + \tfrac{p}{\rho}, u\right), \frac{\partial G}{\partial \mathbf{W}} = \left(-u^3 + uc^2, \tfrac{3}{2}u^2 + \tfrac{p}{\rho}\right),$$

$$\partial_2 G = Q\frac{\partial_2 p}{\rho}, \frac{\partial \mathbf{F}}{\partial W} = \begin{pmatrix} 0 & 1 \\ c^2 - u^2 & 2u \end{pmatrix}, \mathbf{S} - \partial_2 \mathbf{F} = \begin{pmatrix} 0 \\ -\frac{A}{\rho}\partial_2 p \end{pmatrix},$$

and the conditions in (16) are satisfied. For the blood flow model, let us consider the case where the pressure $p = p(A)$ is an explicit function of A. One can provide a large class of entropy-satisfying semi-discrete numerical schemes as follows. Let us consider a numerical flux of the form

$$\mathbf{F}_{j+\frac{1}{2}} = \mathscr{F}\left(\overline{\mathbf{W}}_j, \overline{\mathbf{W}}_{j+1}\right) - a_{j+\frac{1}{2}}\left(\overline{\mathbf{W}}_{j+1} - \overline{\mathbf{W}}_j\right), \tag{21}$$

where $\mathscr{F}(\overline{\mathbf{W}}_j, \overline{\mathbf{W}}_{j+1})$ is a second (or higher) order approximation of the flux at the cell interface $s_{j+\frac{1}{2}}$, and $a_{j+\frac{1}{2}}$ is a free viscosity parameter that does not appear explicitly in the numerical flux $\mathscr{F}\left(\overline{\mathbf{W}}_j, \overline{\mathbf{W}}_{j+1}\right)$. This condition on $a_{j+\frac{1}{2}}$ will be clarified below. Let us also take a second-order approximation $\mathscr{G}(\overline{\mathbf{W}}_j, \overline{\mathbf{W}}_{j+1})$ of $G(\mathbf{W})$ at $s_{j+\frac{1}{2}}$, such that

$$\begin{aligned} \mathbf{R}_j &= \frac{\partial \mathcal{E}}{\partial \mathbf{W}}(\overline{\mathbf{W}}_j) \cdot \left(\mathscr{F}\left(\overline{\mathbf{W}}_j, \overline{\mathbf{W}}_{j+1}\right) - \mathscr{F}\left(\overline{\mathbf{W}}_{j-1}, \overline{\mathbf{W}}_j\right) - \Delta s \bar{\mathbf{S}}_j\right) - \left(\mathscr{G}\left(\overline{\mathbf{W}}_j, \overline{\mathbf{W}}_{j+1}\right) - \mathscr{G}\left(\overline{\mathbf{W}}_{j-1}, \overline{\mathbf{W}}_j\right)\right) \\ &= O(\Delta s^2) \end{aligned} \tag{22}$$

is at least of order $O(\Delta s^2)$. The following proposition provides us with a condition for the vanishing viscosity $a_{j+\frac{1}{2}}$ to guarantee that the semi-discrete numerical scheme is entropy-satisfying.

Proposition 4. Let us consider the semi-discrete numerical scheme using numerical flux (21) associated with system (1) when $p = p(A)$, with conserved variables, flux, and source terms given by equations (19) and (20). The numerical scheme is entropy-satisfying provided that

$$a_{j\pm\frac{1}{2}} \geq \frac{-2\mathbf{R}_j\left(\overline{\mathbf{W}}_{j-1}, \overline{\mathbf{W}}_j, \overline{\mathbf{W}}_{j+1}\right)}{\frac{A_j + A_{j+1}}{2}\left(u_{j+1} - u_j\right)^2 + \frac{A_j + A_{j-1}}{2}\left(u_j - u_{j-1}\right)^2 + \frac{p(A_{j+1}) - p(A_j)}{\rho}(A_{j+1} - A_j) + \frac{p(A_j) - p(A_{j-1})}{\rho}(A_j - A_{j-1})}. \tag{23}$$

Note: Because $p = p(A)$ is an increasing function of $A > 0$, the denominator is non-negative and it vanishes only in the trivial case where $A_{j-1} = A_j = A_{j+1}, u_{j-1} = u_j = u_{j+1}$. In such a situation, $\mathbf{R}_j = 0$, and one can take $a_{j\pm\frac{1}{2}} = 0$.

Proof. Let us denote by $\mathcal{E}_A = -\frac{1}{2}u^2 + \frac{p}{\rho}$ and $\mathcal{E}_Q = u$ the derivatives of the entropy function with respect to the conserved variables. We note that we can decompose

$$\begin{aligned}
&\mathcal{E}_{A_j}(A_{j+1} - A_j) + \mathcal{E}_{Q_j}(Q_{j+1} - Q_j) \\
&\quad = \tfrac{\mathcal{E}_{A_j}+\mathcal{E}_{A_{j+1}}}{2}(A_{j+1} - A_j) + \tfrac{\mathcal{E}_{Q_j}+\mathcal{E}_{Q_{j+1}}}{2}(Q_{j+1} - Q_j) - \tfrac{\mathcal{E}_{A_{j+1}}-\mathcal{E}_{A_j}}{2}(A_{j+1} - A_j) - \tfrac{\mathcal{E}_{Q_{j+1}}-\mathcal{E}_{Q_j}}{2}(Q_{j+1} - Q_j) \\
&\quad = \tfrac{\mathcal{E}_{A_j}+\mathcal{E}_{A_{j+1}}}{2}(A_{j+1} - A_j) + \tfrac{\mathcal{E}_{Q_j}+\mathcal{E}_{Q_{j+1}}}{2}(Q_{j+1} - Q_j) - \tfrac{1}{2}\left(\tfrac{A_j+A_{j+1}}{2}(u_{j+1} - u_j)^2 + \tfrac{p(A_{j+1})-p(A_j)}{\rho}(A_{j+1} - A_j)\right),
\end{aligned} \tag{24}$$

and similarly

$$\begin{aligned}
&\mathcal{E}_{A_j}(A_j - A_{j-1}) + \mathcal{E}_{Q_j}(Q_j - Q_{j-1}) \\
&\quad = \tfrac{\mathcal{E}_{A_{j-1}}+\mathcal{E}_{A_j}}{2}(A_j - A_{j-1}) + \tfrac{\mathcal{E}_{Q_{j-1}}+\mathcal{E}_{Q_j}}{2}(Q_j - Q_{j-1}) + \tfrac{\mathcal{E}_{A_j}-\mathcal{E}_{A_{j-1}}}{2}(A_j - A_{j-1}) + \tfrac{\mathcal{E}_{Q_j}-\mathcal{E}_{Q_{j-1}}}{2}(Q_j - Q_{j-1}) \\
&\quad = \tfrac{\mathcal{E}_{A_{j-1}}+\mathcal{E}_{A_j}}{2}(A_j - A_{j-1}) + \tfrac{\mathcal{E}_{Q_{j-1}}+\mathcal{E}_{Q_j}}{2}(Q_j - Q_{j-1}) + \tfrac{1}{2}\left(\tfrac{A_{j-1}+A_j}{2}(u_j - u_{j-1})^2 + \tfrac{p(A_j)-p(A_{j-1})}{\rho}(A_j - A_{j-1})\right).
\end{aligned} \tag{25}$$

Defining

$$G_{j+\frac{1}{2}} = \mathscr{G}\left(\overline{\mathbf{W}}_j, \overline{\mathbf{W}}_{j+1}\right) - a_{j+\frac{1}{2}}\left[\frac{\mathcal{E}_{A_j} + \mathcal{E}_{A_{j+1}}}{2}(A_{j+1} - A_j) + \frac{\mathcal{E}_{Q_j} + \mathcal{E}_{Q_{j+1}}}{2}(Q_{j+1} - Q_j)\right],$$

we obtain

$$\begin{aligned}
&\tfrac{\partial \mathcal{E}}{\partial \mathbf{W}}(\overline{\mathbf{W}}_j) \cdot \left(\mathbf{F}_{j+\frac{1}{2}} - \mathbf{F}_{j-\frac{1}{2}} - \Delta s \bar{\mathbf{S}}_j\right) - (G_{j+\frac{1}{2}} - G_{j-\frac{1}{2}}) \\
&= \mathbf{R}_j + \tfrac{a_{j+\frac{1}{2}}}{2}\left(\tfrac{A_j+A_{j+1}}{2}(u_{j+1} - u_j)^2 + \tfrac{p(A_{j+1})-p(A_j)}{\rho}(A_{j+1} - A_j)\right) + \tfrac{a_{j-\frac{1}{2}}}{2}\left(\tfrac{A_{j-1}+A_j}{2}(u_j - u_{j-1})^2 + \tfrac{p(A_j)-p(A_{j-1})}{\rho}(A_j - A_{j-1})\right),
\end{aligned} \tag{26}$$

which concludes the proof. □

High resolution numerical schemes, such as central or central-upwind schemes, use numerical fluxes of the form $\mathscr{F}\left(\mathbf{W}^-_{j+\frac{1}{2}}, \mathbf{W}^+_{j+\frac{1}{2}}\right) - a_{j+\frac{1}{2}}(\mathbf{W}^+_{j+\frac{1}{2}} - \mathbf{W}^-_{j+\frac{1}{2}})$, where $\mathbf{W}^\pm_{j+\frac{1}{2}}$ are reconstructed values at the cell interfaces. However, such schemes reduce to first-order accurate schemes near shock waves, where we actually need the entropy inequality. In smooth regions, equation (15) is satisfied as an equality in the continuous limit. Near shock waves or local singularities, the minmod local reconstruction is trivial, and the vanishing viscosity term reduces to the form of equation (21).

In smooth regions, condition (23) can be rewritten as

$$a_{j\pm\frac{1}{2}} \geq \frac{-2\frac{\mathbf{R}_j}{\Delta s^2}\left(\overline{\mathbf{W}}_{j-1}, \overline{\mathbf{W}}_j, \overline{\mathbf{W}}_{j+1}\right)}{\frac{A_j+A_{j+1}}{2}\left(\frac{u_{j+1}-u_j}{\Delta s}\right)^2 + \frac{A_j+A_{j-1}}{2}\left(\frac{u_j-u_{j-1}}{\Delta s}\right)^2 + \frac{p(A_{j+1})-p(A_j)}{\rho\Delta s}\frac{A_{j+1}-A_j}{\Delta s} + \frac{p(A_j)-p(A_{j-1})}{\rho\Delta s}\frac{A_j-A_{j-1}}{\Delta s}},$$

which is bounded as $\Delta s \to 0$. Near discontinuities, the right hand side is of order 1. In any case, the condition is not too restrictive. In fact, for the special case where the pressure is given by equation (2), $\beta = 2, G_o, A_o$ constants, we have

$$\begin{aligned}
R_j &= \tfrac{1}{4}\left[A_{j-1}u_{j-1}(u_j - u_{j-1})^2 - A_{j+1}u_{j+1}(u_{j+1} - u_j)^2\right] + \tfrac{G_o}{4A_oA_j\rho}\left[A_{j-1}u_{j-1}(A_{j+1} - A_{j-1})(A_{j+1} - 2A_j + A_{j-1})\right. \\
&\left. -2A_j(A_{j+1} - A_j)(A_{j+1}u_{j+1} - A_{j-1}u_{j-1}) + (A_{j+1} + A_{j-1})(A_{j+1} - A_{j-1})(A_ju_j - A_{j-1}u_{j-1})\right],
\end{aligned} \tag{27}$$

which is actually of order $O(\Delta s^3)$ as $\Delta s \to 0$ in smooth regions, making the right hand side of equation (23) of order $O(\Delta s)$.

3.3 | Semi-discrete central-upwind scheme

The semi-discrete formulation for the cell averages as in (17) is obtained after integrating equation (14) over each cell I_j, obtaining equation (18). The semi-discrete formulation is approximated by

$$\frac{d}{dt}\overline{\mathbf{W}}_j(t) = -\frac{\mathbf{H}_{j+\frac{1}{2}} - \mathbf{H}_{j-\frac{1}{2}}}{\Delta s} + \frac{1}{\Delta s}\int_{s_{j-\frac{1}{2}}}^{s_{j+\frac{1}{2}}} \mathbf{S}(\mathbf{W}, s)\, ds, \tag{28}$$

where $\mathbf{H}_{j\pm\frac{1}{2}}$ is the numerical flux at the cell interface $s_{j\pm\frac{1}{2}}$. Typical semi-discrete central-upwind schemes consider flux values at the interfaces obtained by non-oscillatory polynomial reconstructions. Non-oscillatory behavior is usually achieved by the use of nonlinear limiters, as described in [27].

The flux at the cell interfaces, $\mathbf{F}(\mathbf{W}(s_{j\pm\frac{1}{2}}), t)$, is approximated by the numerical flux $\mathbf{H}_{j\pm\frac{1}{2}}(t)$ given by

$$\mathbf{H}_{j\pm\frac{1}{2}}(t) = \frac{a^+_{j\pm\frac{1}{2}}\mathbf{F}\left(\mathbf{W}^-_{j\pm\frac{1}{2}}(t)\right) - a^-_{j\pm\frac{1}{2}}\mathbf{F}\left(\mathbf{W}^+_{j\pm\frac{1}{2}}(t)\right)}{a^+_{j\pm\frac{1}{2}} - a^-_{j\pm\frac{1}{2}}} + \frac{a^+_{j\pm\frac{1}{2}}a^-_{j\pm\frac{1}{2}}}{a^+_{j\pm\frac{1}{2}} - a^-_{j\pm\frac{1}{2}}}\left(\mathbf{W}^+_{j\pm\frac{1}{2}}(t) - \mathbf{W}^-_{j\pm\frac{1}{2}}(t)\right). \tag{29}$$

The numerical flux is of HLL type, as described in [47]. The interface point-values $\mathbf{W}^{\pm}_{j\pm\frac{1}{2}}(t)$ are recovered from the cell averages via a non-oscillatory piecewise polynomial reconstruction that is described in the next section. The one-sided local speeds in this scheme are approximated using the eigenvalues of the Jacobian:

$$\begin{aligned}
a^-_{j\pm\frac{1}{2}} &= \min\left\{\alpha u^+_{j\pm\frac{1}{2}} - \sqrt{\alpha(\alpha-1)\left(u^+_{j\pm\frac{1}{2}}\right)^2 + \left(c^+_{j\pm\frac{1}{2}}\right)^2}, \alpha u^-_{j\pm\frac{1}{2}} - \sqrt{\alpha(\alpha-1)\left(u^-_{j\pm\frac{1}{2}}\right)^2 + \left(c^-_{j\pm\frac{1}{2}}\right)^2}, 0\right\},\\
a^+_{j\pm\frac{1}{2}} &= \max\left\{\alpha u^+_{j\pm\frac{1}{2}} + \sqrt{\alpha(\alpha-1)\left(u^+_{j\pm\frac{1}{2}}\right)^2 + \left(c^+_{j\pm\frac{1}{2}}\right)^2}, \alpha u^-_{j\pm\frac{1}{2}} + \sqrt{\alpha(\alpha-1)\left(u^-_{j\pm\frac{1}{2}}\right)^2 + \left(c^-_{j\pm\frac{1}{2}}\right)^2}, 0\right\}.
\end{aligned} \tag{30}$$

We note that $a^+_{j\pm\frac{1}{2}} - a^-_{j\pm\frac{1}{2}} > 0$ is always positive unless $A^{\pm}_{j\pm\frac{1}{2}}$ and $u^{\pm}_{j\pm\frac{1}{2}}$ all vanish in a collapsed state with "no fluid motion". However, we always start with positive but possibly small values of A.

3.4 | Positivity-preserving non-oscillatory reconstruction

The construction of a numerical scheme that is second-order accurate in smooth regions is one of the goals in this work. The numerical scheme becomes first-order accurate near shock waves to achieve stability. The interface point values $\mathbf{W}_{j\pm\frac{1}{2}}(t)$ are calculated from the cell averages $\overline{\mathbf{W}}_j(t)$ via piecewise polynomial reconstruction. For that end, the reconstruction implemented here conserves cell averages, is second-order accurate in smooth regions, has a non-oscillatory behaviour, recognizes steady states at rest, and preserves the positivity of the cross-sectional area A. See references [48,49,50,51] for details.

A second-order reconstruction of any quantity $q(s,t)$ is chosen from its cell average $\bar{q}_j$ as

$$q^+_{j-\frac{1}{2}} = \bar{q}_j - \frac{\Delta s}{2}q'_j, \quad q^-_{j+\frac{1}{2}} = \bar{q}_j + \frac{\Delta s}{2}q'_j. \tag{31}$$

The *limited* slopes q'_j are calculated according to reference [52] as

$$q'_j = \frac{1}{\Delta s}\text{minmod}\left(\theta\left(\overline{q}_j - \overline{q}_{j-1}\right), \frac{1}{2}\left(\overline{q}_{j+1} - \overline{q}_{j-1}\right), \theta\left(\overline{q}_{j+1} - \overline{q}_j\right)\right), \tag{32}$$

where $1 \le \theta < 2$, and

$$\text{minmod}(r_1, r_2, r_3, \ldots, r_k) = \begin{cases} \min_j(r_j) & \text{if } r_j > 0\ \forall j \\ \max_j(r_j) & \text{if } r_j < 0\ \forall j \\ 0 & \text{otherwise} \end{cases}.$$

Unless otherwise specified, $\theta = 1.5$. We note that this minmod limiter is commonly used in central-upwind schemes. It guarantees the local maximum principle with respect to the cell averages [27].

Steady state at rest and positivity of cross-sectional area

The interface data is constructed as follows. The quantity $A_o(s)$ and the pressure are defined at $s_{j\pm\frac{1}{2}}$, and at each cell center, both quantities are calculated as

$$A_{o,j} = \frac{A_{o,j-\frac{1}{2}} + A_{o,j+\frac{1}{2}}}{2}, \quad p_{j\pm\frac{1}{2}}(A) = p(A, s_{j\pm\frac{1}{2}}), \quad p_j(A) = \frac{p_{j-\frac{1}{2}}(A) + p_{j+\frac{1}{2}}(A)}{2}.$$

Removing the overbar $\bar{A}_j = A_j$ for the cell averages, we compute the re-scaled values $\mathbb{A}_j = A_j/A_{o,j}$ inside each cell. One then reconstructs $\mathbb{A}^{\pm}_{j\pm\frac{1}{2}}$ according to (31) to recover

$$A^{\pm}_{j\pm\frac{1}{2}} = A_{o,j\pm\frac{1}{2}} \mathbb{A}^{\pm}_{j\pm\frac{1}{2}}. \tag{33}$$

We require a trivial reconstruction for steady states at rest ($\mathbb{A} = 1$). Therefore, if we start with a steady state $A_j = A_{o,j}$ $\forall j$, the reconstructions $A^{\pm}_{j+\frac{1}{2}} = A_{o,j+\frac{1}{2}}$ are trivial. This procedure will be helpful in achieving the well-balanced property.

Note: It is well-known that if the cross-sectional areas A_j in each cell I_j are positive, so are the reconstructions $A^{\pm}_{j\pm\frac{1}{2}}$.

3.5 | Well-balanced property

Steady state at rest may also occur for tilted vessels, and the cross-sectional area satisfies $p(A, s) + g\rho z(s) = \text{const}$. In the tilted case, the relation $A = A_o(s)$ does not correspond to a steady state, and the reconstruction is more complicated. In this section, we assume $\theta(s) = 0$ for simplicity. The well-balanced property has been shown to improve the accuracy of the scheme near steady-state flows[53,44,54,55]. Let us consider a steady state at rest, *i.e.*, $A_j = A_{o,j}$ and $Q_j = 0$ for all j. Then, the reconstructed point values $A^{\pm}_{j\pm\frac{1}{2}}$ given by (33), will trivially yield $\bar{A}_j(t + \Delta t) = \bar{A}_j(t)$.

For the momentum equation, the cell average of the source term $\overline{\mathbf{S}}_j$ in (20) must be discretized to balance the numerical fluxes (29). Under the above conditions, the minmod reconstruction of Q and A/A_o is trivial ($(\cdot)^-_{j+\frac{1}{2}} = (\cdot)^+_{j+\frac{1}{2}} = (\cdot)_{j+\frac{1}{2}}$), and the $\pm$ signs will be dropped in those cases. On the other hand, the quantity $\bar{p}(A, s)$ appearing as a source term satisfies

$$\partial_2 \bar{p} = \frac{1}{A}\int_{A_o(s)}^{A(s,t)} \partial_2 p(\mathcal{A}, s) d\mathcal{A} - \frac{1}{A} p(A_o(s), s) A_o'(s) = \frac{1}{A}\int_{A_o(s)}^{A(s,t)} \partial_2 p(\mathcal{A}, s) d\mathcal{A},$$

which clearly vanishes when $A = A_o$. One must find a second-order discretization that vanishes when $A = A_o$. One then approximates the source terms in equation (20) as

$$\frac{1}{\Delta s}\int_{s_{j-\frac{1}{2}}}^{s_{j+\frac{1}{2}}} 2\frac{\alpha\nu u}{\alpha - 1}\, ds \approx 2\frac{\alpha\nu}{\alpha - 1}\frac{u^+_{j-\frac{1}{2}} + u^-_{j+\frac{1}{2}}}{2}, \tag{34}$$

$$\frac{1}{\Delta s}\int_{s_{j-\frac{1}{2}}}^{s_{j+\frac{1}{2}}} \frac{A}{\rho}\partial_2 p(A(s,t), s) ds \approx \frac{A^+_{j-\frac{1}{2}} + A^-_{j+\frac{1}{2}}}{2\rho}\left(\frac{1}{2}\int_{A_{o,j-\frac{1}{2}}}^{A^+_{j-\frac{1}{2}}} \partial_2 p(\mathcal{A}, x_j) d\mathcal{A} + \frac{1}{2}\int_{A_{o,j+\frac{1}{2}}}^{A^-_{j+\frac{1}{2}}} \partial_2 p(\mathcal{A}, x_j) d\mathcal{A}\right). \tag{35}$$

If the pressure $p = p(A, s)$ has an explicit expression as in equation (2), the integral in the last expression could be computed explicitly or a trapezoidal rule could be used to approximate such an integral. If the pressure is only available at the cell interfaces, one could also use the approximation $\partial_2 p(A, x_j) = (p(A, s_{j+\frac{1}{2}}) - p(A, s_{j-\frac{1}{2}}))/\Delta s$. One does not expect to have strong differences in the numerical results with either choice if the well-balanced property is maintained.

The well-balanced property is described in the following proposition.

Proposition 5. Let $A_{o,j\pm\frac{1}{2}} = A_o(s_{j\pm\frac{1}{2}})$ be the unstressed area at the interfaces $s_{j\pm\frac{1}{2}}$. Let us define the source terms approximations in (20) according to (34) and (35). Then, the scheme (28) - (29) with the above approximation is well balanced, i.e., $\frac{d}{dt}\overline{\mathbf{W}}_j(t) = 0$ for steady states at rest.

The proof is standard. The details can be found in[49,50].

3.6 | Evolution in time

The time integration of the ODE system (28) is done using the second-order strong stability preserving Runge-Kutta scheme[56]

$$\mathbf{W}^{(1)} = \mathbf{W}^{(0)} + \Delta t\, \mathbf{C}[\mathbf{W}^{(0)}] \tag{36a}$$

$$\mathbf{W}^{(2)} = \frac{1}{2}\mathbf{W}^{(0)} + \frac{1}{2}\left(\mathbf{W}^{(1)} + \Delta t\, \mathbf{C}[\mathbf{W}^{(1)}]\right) \tag{36b}$$

$$\overline{\mathbf{W}}(t+\Delta t) := \mathbf{W}^{(2)}, \tag{36c}$$

with

$$\mathbf{C}[\mathbf{W}(t)] = -\frac{\mathbf{H}_{j+\frac{1}{2}}(\mathbf{W}(t)) - \mathbf{H}_{j-\frac{1}{2}}(\mathbf{W}(t))}{\Delta s} + \overline{\mathbf{S}}_j(t), \tag{37}$$

and $\overline{\mathbf{S}}_j(t)$ calculated according to (34) - (35). The *CFL* condition that determines the time step Δt is

$$\frac{a\Delta t}{\Delta s} \leq \frac{1}{2}, \tag{38}$$

where $a = \max_j \max(a^+_{j\pm\frac{1}{2}}, -a^-_{j\pm\frac{1}{2}})$.

The following proposition shows that this *CFL* condition guarantees the positivity of the cross-sectional area A when the solution is computed with the Runge-Kutta method (36).

Proposition 6. Consider the scheme (28)- (29) with the reconstruction algorithm described in §3.4 and the discretization of the source term (34) - (35) . If the cell averages $\bar{A}(t)$ are such that

$$\bar{A}_j(t) > 0 \quad \forall j,$$

then the cell averages $\bar{A}(t+\Delta t)$ computed with the Runge-Kutta method (36) under the *CFL* limitation (38) will yield

$$\bar{A}_j(t+\Delta t) \geq 0 \ \forall j.$$

The proof is standard. The details can be found in[49,50].

4 | NUMERICAL RESULTS

In this section, we present several numerical tests to verify the properties of the proposed numerical scheme. The numerical tests are performed for the special case where the pressure is given by equation (2). The stress-strain response is given by $\beta = 2$ and the density is $\rho = 1050\ \text{kg m}^{-3}$ in all the numerical tests.

Here, we employ exact solutions of the Riemann problem to analyze the order of accuracy of the numerical approximations as follows. Given a non-vanishing quantity q in the domain $[s_o, s_1]$, which is an approximation to the quantity q_{exact}, the relative absolute error is defined as

$$E_q(t) := \frac{1}{L}\int_{s_o}^{s_1} \frac{|q(s,t) - q_{\text{exact}}(s,t)|}{|q_{\text{exact}(s,t)}|} ds. \tag{39}$$

In this work, we take $q = R$, the vessel's radius. It does not vanish, and the above expression is valid.

4.1 | A Riemann problem

In this test, we set the model parameters as in[4]. The elasticity coefficient is $G_o = 40\ \text{k Pa}$. The Young's modulus is $E_Y = 300\ \text{k Pa}$, and the corresponding wall thickness is $h_d = R_o/10$. The unstressed cross-sectional area is $A_o = 2.1\ \text{cm}^2$, which corresponds to an unstressed radius of $R_0 = 0.82\ \text{cm}$. The viscosity coefficient is set to zero ($\nu = 0$) and $\alpha = 1$. In the case of a horizontal vessel, the arc length position s coincides with the horizontal position x. To distinguish horizontal from tilted vessels, we will use the variable x when $\theta = 0$.

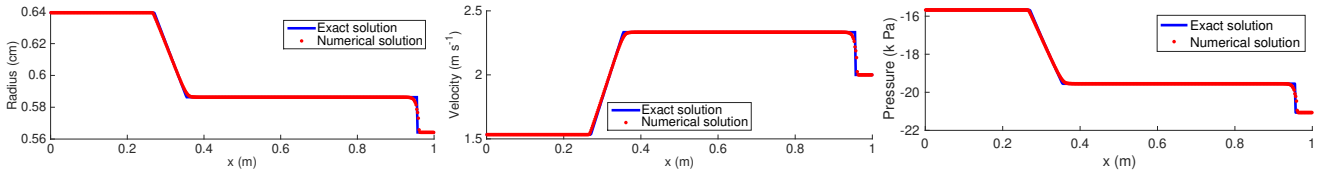

FIGURE 2 Riemann problem corresponding to the initial conditions reported in (40) at time $t = 0.07$ s. The vessel's radius (in cm) is displayed in the left panel, the velocity in units of m s^{-1} in the middle panel, and the pressure is shown in the right panel. The exact solution is denoted by a solid blue line, and the numerical approximation is indicated by the dotted red line.

The domain in this numerical test is [0 m, 1 m]. We consider the following initial conditions associated with a Riemann problem:

$$(A,u)(x,0) = \begin{cases} (1.28\ \text{cm}^2, 1.53\ \text{ms}^{-1}), & \text{if } \ 0 \le x < 0.5\ \text{m}. \\ \\ (1\ \text{cm}^2, 0.63\ \text{ms}^{-1}), & \text{if } \ 0.5\ \text{m} \le x \le 1\ \text{m}. \end{cases} \tag{40}$$

The left state corresponds to a radius of $R_\ell = 0.64$ cm, while the right one decreases to $R_r = 0.5642$ cm. The initial condition corresponds to a Riemann problem with solution consisting of a left going rarefaction wave and a right shock wave. The middle state is $(R_m = 0.586\ \text{cm}, u_m = 2.33\ \text{ms}^{-1})$. The exact solution was constructed with the above procedure, and the results are displayed in Figure 2. In the figure, the numerical approximation is shown at time $t = 0.07$ s, and it was obtained with the central-upwind scheme described in Section 3 using a grid resolution of 500 grid points and free boundary conditions. The left panel displays the exact (solid blue line) and numerical (dotted red line) radii, while the middle panel shows the velocity. Both variables exhibit very good agreement with the exact solution. The numerical solution is also accurate near the right shock wave. No spurious oscillations are observed. The numerical smearing near the discontinuity is typical in many numerical methods and is moderate in the present case. The relative error given by equation (39) is 3.17×10^{-4} for the radius and 1.4×10^{-3} for the velocity. The right panel of Figure 2 shows the transmural pressure, which decreases with respect to x at a given time. Because the pressure is higher at the left end, the fluid is pushed towards the right. As a result, the velocity is positive and increases across the rarefaction where the artery's cross section decreases. All variables decrease again across the right-going shock wave.

The proposed numerical scheme is formally second-order accurate in smooth regions and first-order accurate near discontinuities. One can verify the rate of convergence when the exact solution is available, as in the Riemann problem. The left panel of Figure 3 shows the log-log plot of the numerical error versus Δx for different grid resolutions. The radius is the variable employed here to compute the relative error. Because the solution involves shock waves, the approximation is first-order accurate near discontinuities. The red asterisks are close to the blue line with slope 1 in the log-log plot. The error was taken at time $t = 0.07$ s over the domain [0 m, 1 m]. The right panel repeats the computation when the numerical error is computed inside the rarefaction wave and when the initial conditions are the Riemann solution at time $t_o = 0.15T = 0.0105$ s, instead of piecewise constant initial conditions. Otherwise, the initial discontinuity may affect the accuracy of the numerical approximation. The numerical error is computed at the same final time $t = 0.07$ s, starting at $t_o = 0.0105$ s, and the integral is taken over the spatial portion of the domain [0.28 m, 0.34 m], which corresponds to a portion inside the rarefaction where the solution is smooth. In this case, the solution involves no discontinuities, and the log-log plot confirms a second-order approximation.

4.2 | Numerical test for the positivity preserving property

The numerical scheme presented here is positivity-preserving according to Proposition 6. We numerically test this property in this section. To this end, we consider a Riemann problem with initial conditions

$$(A,u)(x,0) = \begin{cases} (0.1596\ \text{cm}^2, 1\ \text{ms}^{-1}), & \text{if } \ 0 \le x < 0.5\ \text{m}. \\ \\ (0.5\ \text{cm}^2, -8.279\ \text{ms}^{-1}), & \text{if } \ 0.5\ \text{m} \le x < 1\ \text{m}. \end{cases} \tag{41}$$

Here, $\nu = 0, \alpha = 1, G_o = 40$ k Pa, and $R_o = 0.82$ cm. The solution to this Riemann problem consists of two rarefaction waves connected to an intermediate state $(A_m, u_m) = (5 \times 10^{-5}\ \text{cm}^2, -4.9456\ \text{ms}^{-1})$. The remaining parameter values are taken from the previous example.

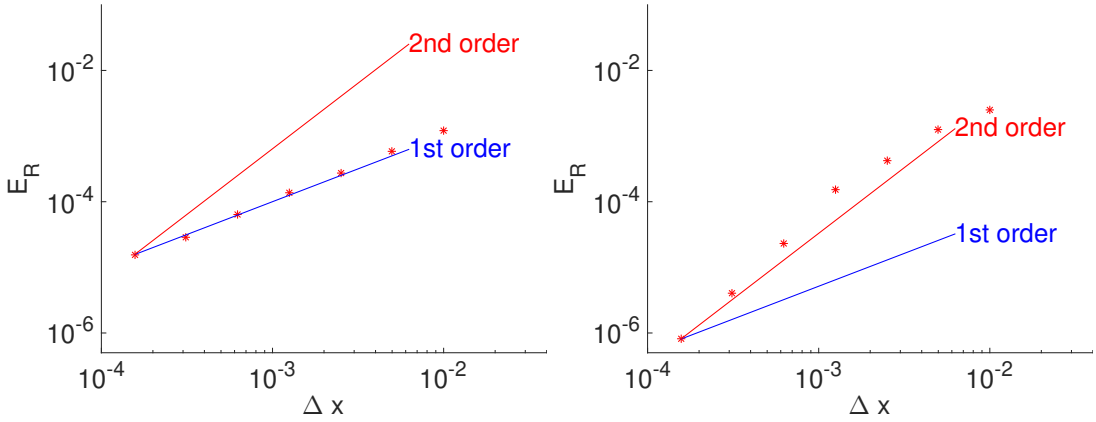

FIGURE 3 Left: Log-log plot of numerical error for the radius E_R calculated according to equation (39) versus Δx (red asterisks) for the numerical solution at time $t = 0.07$ s with initial conditions (40) using $N = 100, 100 \times 2, \ldots, 100 \times 2^6$ grid points. Right: The same numerical error computed in the region $[0.28, 0.34]$ when the initial condition is the solution to the Riemann problem at $t_o = 0.0105$ s and the end time is $t = 0.07$ s. The red and blue lines have slopes 2 and 1 in the log-log plot, respectively.

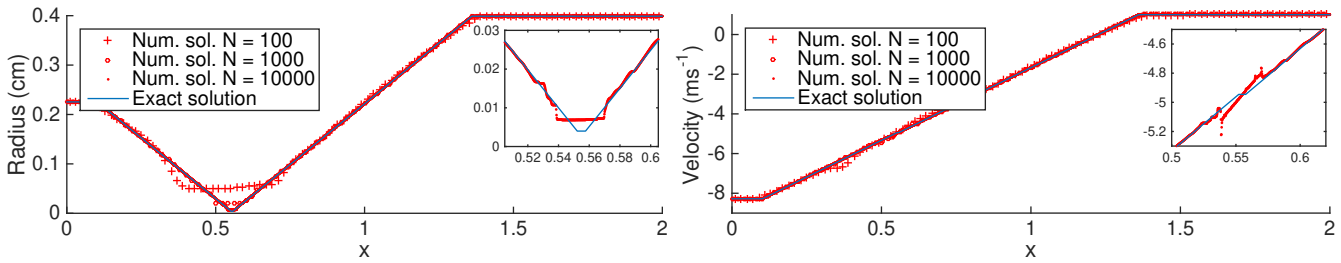

FIGURE 4 Exact (blue line) and numerical approximations (dotted red line) of the radius (left panel) and velocity (right panel) at time $t = 0.09$ s. The initial conditions are given by (41). An inset with a zoom near the intermediate state is also shown in each panel.

Figure 4 shows the exact solution (blue line) and numerical predictions (dotted red line) for the radius (left panel) and velocity (right panel) at $t = 0.09$ s. Here, we use free boundary conditions. We note that the intermediate state is much smaller with reference to the left and right states, as in a vacuum problem. The computation of the eigenvalues in the numerical algorithm requires the square root of the cross-sectional area. A numerical complication arises when numerical errors lead to negative values of the approximated cross-sectional area. The positivity-preserving property is important to correctly compute the solution near the intermediate small state. The agreement is very good, except for a very small oscillation in the velocity near the rarefaction edges. The intermediate state covers a very small portion of the domain. Numerical difficulties are anticipated in those cases (see Fig. 11 in[57]), and a very fine grid resolution is required to improve the accuracy near that state. The numerical solution is computed using 100 grid points ("+" signs), 1,000 grid points ("o" signs), and 10,000 grid points (dotted line in Figure 4). We clearly observe the improvement in the numerical approximation near the intermediate state as we increase the grid resolution. An inset with a zoom of the intermediate state is shown in each panel. The numerical errors are more visible in this inset. Such errors near rarefaction edges are common in many numerical schemes. The relative errors given by equation (39) are 2.27×10^{-1}, 5.12×10^{-2}, and 6.2×10^{-3} for the radius and 2.26×10^{-2}, 3.6×10^{-3}, and 4.1×10^{-4} for the velocity, respectively.

We illustrate the importance of the positivity-preserving property by showing that we may obtain negative values of A when it is not implemented. Here, we use a regular central scheme without the positivity-preserving property, using a CFL number of 0.9 and 500 grid points. When the cross-sectional area becomes negative, we correct it increasing it to a threshold 10^{-10} m^2 to avoid serious numerical complications. Figure 5 shows numerical profiles of radius (top left) and velocity (top right) at time $t = 0.004$ s.

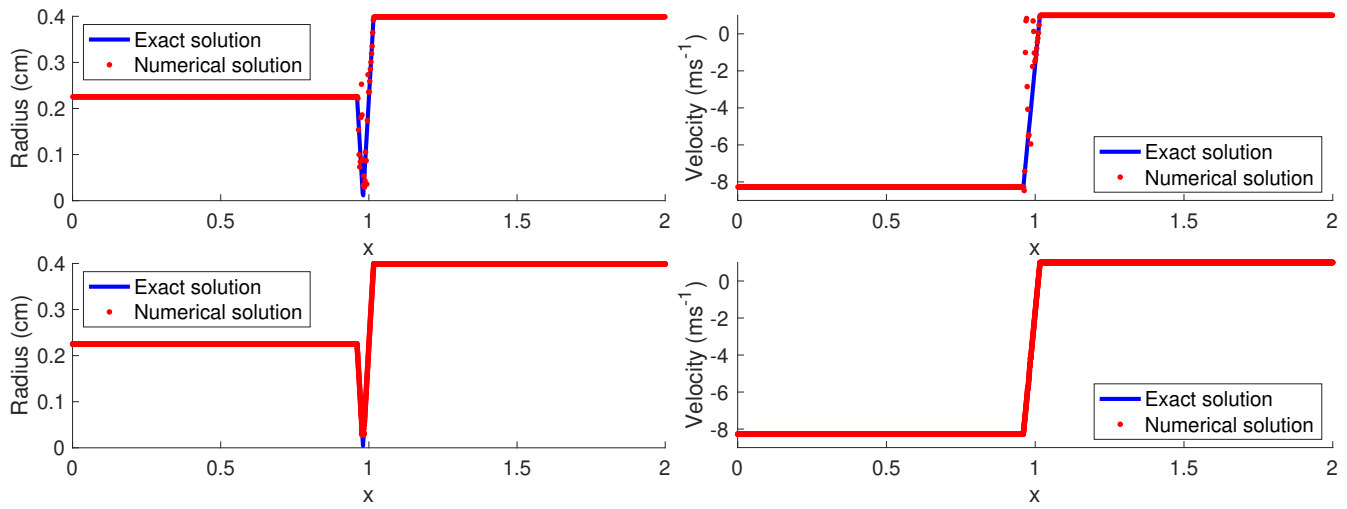

FIGURE 5 Top panels: exact (blue line) and numerical approximations (dotted red line) of the radius (top left panel) and velocity (top right panel) at time $t = 0.004$ s using a numerical scheme that is not positivity preserving. The initial conditions are given by (41). Bottom panels: the same as in the top panels but using the numerical scheme proposed here.

One can observe instabilities in the numerical solution. We repeated the computations with the positivity-preserving numerical scheme proposed here, and we show the results in the bottom panels. The results are very accurate, except in the intermediate state. Central/upwind schemes are first-order accurate near peaks or discontinuities due to the minmod reconstruction, which is required for stability.

4.3 | Perturbation to a moving steady state

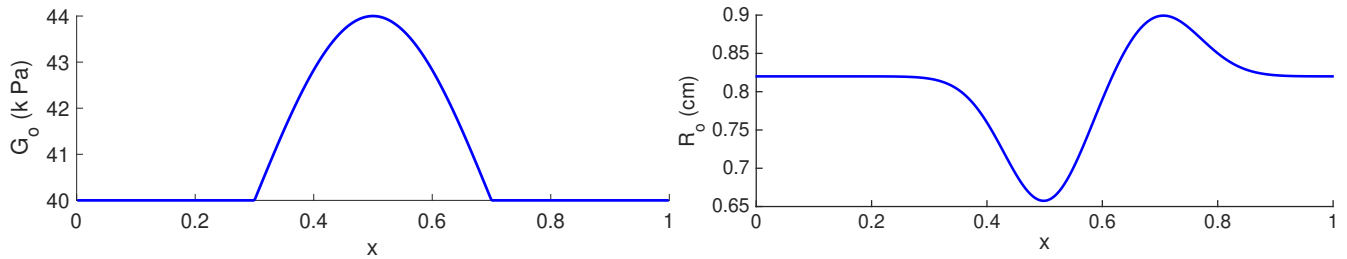

FIGURE 6 Elasticity parameter G_o (left) and unstressed radius R_o (right) as a function of x.

It has been shown in many situations that the flows are small perturbations from steady states[34]. It was shown in Section 3 that the numerical scheme presented here satisfies the well-balanced property. This property improves the accuracy of numerical approximations near steady states[55]. We have characterized the equilibrium solutions in Proposition 2 and the invariant quantities in equation (9), even in the case where the viscosity coefficient is positive. In this section, we take $\alpha = 1.1$, and consider a perturbation to one of those equilibrium solutions in horizontal vessels ($\theta = 0$). The quantities $R_o = R_o(x)$, and $G_o = G_o(x)$ defined in the domain [0 m, 1 m] are given by

$$R_o(x) = 0.82\left(1 - 0.2\exp\left(-100\ \text{m}^{-2}(x - 0.5\ \text{m})^2\right) + 0.1\exp\left(-100\ \text{m}^{-2}(x - 0.75\ \text{m})^2\right)\right)\ \text{cm}, \tag{42}$$

and

$$G_o(x) = \begin{cases} 20\left(1 + 0.1\sin\left(\pi(x\ \mathrm{m}^{-1} - 0.3)/0.4\right)\right)\ \mathrm{k\,Pa} & \text{if } \ 0.3\ \mathrm{m} < x \leq 0.7\ \mathrm{m} \\ 20\ \mathrm{k\,Pa} & \text{if } \ x \in [0, 1\ \mathrm{m}] \setminus [0.3, 0.7\ \mathrm{m}]. \end{cases} \tag{43}$$

Their profiles are shown in Figure 6.

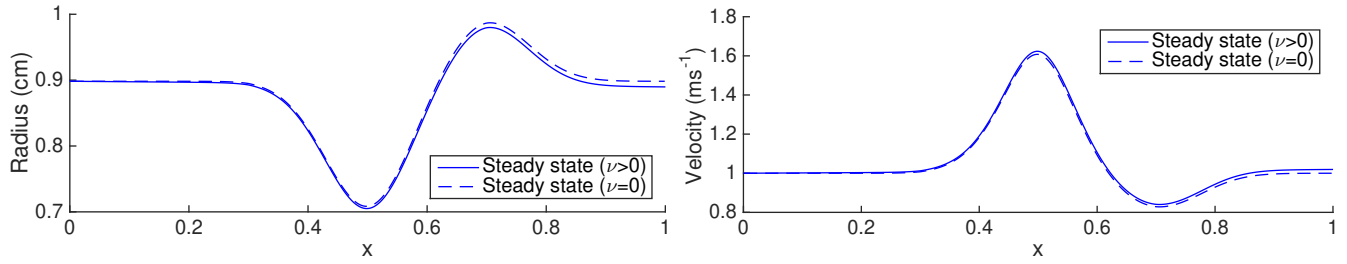

FIGURE 7 Steady-state radius (left) and velocity (right) associated with the boundary data $(R_b, u_b) = (0.82\ \mathrm{cm}, 1.09\ \mathrm{ms}^{-1})$ and parameters given by (42) and (43). The solid blue line is for $\nu = 2.6 \times 10^{-6}\ \mathrm{m}^2\ \mathrm{s}^{-1}$, while the dashed blue line corresponds to $\nu = 0$.

The exact steady states can be computed according to condition (6), even when the viscosity ν is positive. For the above parameters, the exact steady state can be observed in Figure 7. The dashed curve shows the inviscid case, $\nu = 0$, while the solid line was obtained for the value of $\nu = 2.6 \times 10^{-6}\ \mathrm{m}^2\ \mathrm{s}^{-1}$, which is a typical value for blood viscosity at 37° reported in reference[58]. As one can see, the case $\nu > 0$ results in a reduced velocity and increased radius, as expected.

One then considers the steady state $A_{\mathrm{st}}, u_{\mathrm{st}}$ associated to boundary data $(R_b, u_b) = (0.82\ \mathrm{cm}, 1.09\ \mathrm{ms}^{-1})$ at both the left and right boundaries. That is, we start with those values at the left boundary and compute the equilibrium solution in the remainder of the domain according to (6).

We add a perturbation to the steady state according to

$$A(x, 0) = \begin{cases} A_{\mathrm{st}}(x)\left(1 + \frac{1}{2}\sin\left(5\pi\left(x\ \mathrm{m}^{-1} - 0.1\right)\right)\right) & \text{if } \ 0.1 < x \leq 0.3\ \mathrm{m} \\ A_{\mathrm{st}}(x) & \text{otherwise.} \end{cases}$$

Figure 8 shows the evolution of the perturbation (dotted red line) and the steady state (solid blue line). We have used Dirichlet boundary conditions R_b, u_b on both the left and right boundaries. We can observe that the steady state is recovered when the perturbation leaves the domain at $t = 10$ s in spite of the fact that the perturbation is large. The solution is computed for long times until it converges to the initial steady state.

Figure 9 shows the discharge and energy profiles at time $t = 10$ s, which are constant for smooth flows when $\nu = 0$. Here, the discharge is still constant, but the energy decreases as x increases, as expected by Proposition 2. By plotting flat quantities, such as the discharge, we obtain more information about the accuracy of the scheme because we can easily see numerical errors. The top left panel of Figure 9 shows the difference between the steady state discharge (blue solid line) and the numerical solution at $t = 10s$ (red dotted line). The relative absolute errors for Q and E are 1×10^{-3} and 2.56×10^{-4}, respectively. The bottom panels show $|Q - Q_{\mathrm{exact}}|/Q_{\mathrm{exact}}$ and $|E - E_{\mathrm{exact}}|/E_{\mathrm{exact}}$, confirming our observations.

4.4 | Cardiac cycle

The profile shown in Figure 10 is an example of velocity as a function of time imposed at the upstream boundary in a cardiac cycle. The time series was obtained from reference[4], and it was approximated using the first 15 elements of its Fourier decomposition. Initially, the velocity at the left boundary increases up to speeds above 1 ms^{-1}. As a result, the fluid is pushed to the right and shock waves could form in the blood flow, which is an undesired phenomenon.

Shock wave formation inside or outside the physiologically relevant regions was studied in[4]. The physiological relevant domain was defined in[4] as 2.8 m downstream from the inlet boundary. Here, we would like to analyze the effect of varying elastic

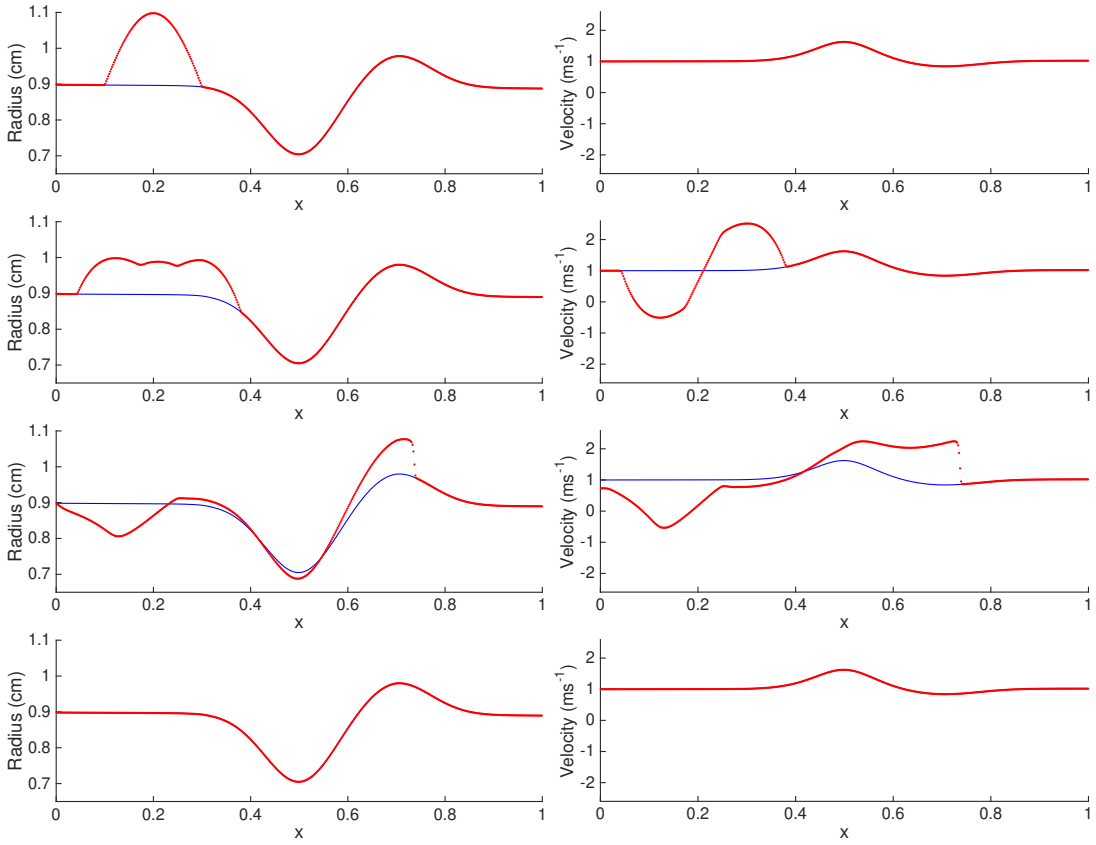

FIGURE 8 Numerical solution at times $t = 0, 0.01, 0.05$, and 10 s in descending order. The initial conditions consists of a perturbation to the steady state with boundary data $(R_b, u_b) = (0.41 \text{ cm}, 1 \text{ ms}^{-1})$ and the quantities R_o, G_o are given by (42) and (43). The left column shows the radius while the right one the velocity of the fluid. The blue solid line corresponds to a steady state and the red dotted line is the evolution of the perturbation.

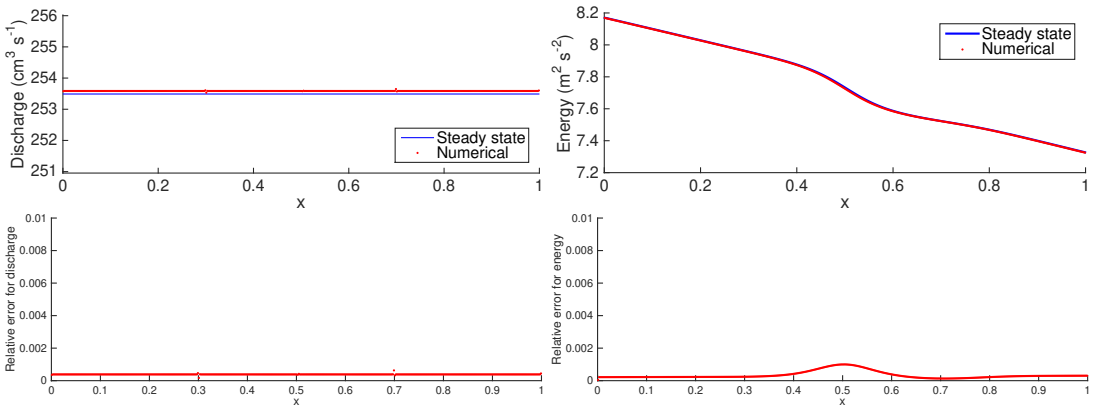

FIGURE 9 Top: Exact steady state (solid blue line) and numerical approximation (red dotted line) of discharge (left) and energy profiles (right) at time $t = 10$ s. Bottom: Relative error for discharge (left) and energy (right).

properties in the artery during the formation of shock waves. Shock wave formation in blood flows could be problematic from a physiological point of view, and it does not happen in healthy individuals. See[59] for an extended analysis. Here, we analyze

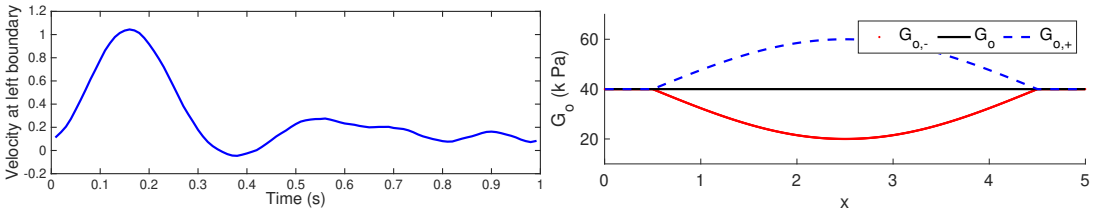

FIGURE 10 Left: Velocity at the left boundary in a cardiac cycle as a function of time. Right: Profiles for G_o (black solid line), $G_{o,-}$ (red dotted line), and $G_{o,+}$ (blue dashed line).

the effect of increasing the rigidity of the walls and study how that can delay or accelerate the formation of a shock wave. The parameters are $g = 9.81$ m s^{-1},$\alpha = 1.1$, $\beta = 2$, $\rho_o = 1050$ kg m^{-3}, and $\nu = 3.2 \times 10^{-6}$ m^2 s^{-1}.

The domain here is $[0, 5$ m$]$. We consider three cases for the elastic properties of the vessel, given by

$$G_o(x) = 4 \times 10^4, \quad G_{o,\pm} = \begin{cases} 40\left(1 \pm \frac{1}{2}\sin\left[\pi\frac{x-\frac{1}{2}}{4}\right)\right] \text{ k Pa} & \text{if } \ 0.5 \text{ m} < x \le 4.5 \text{ m} \\ 40 \text{ k Pa} & \text{if } \ x \in [0, 5 \text{ m}] \setminus [0.5, 4.5 \text{ m}]. \end{cases}$$

A vessel with uniform elasticity is modeled here with the constant parameter G_o. Assuming a constant Young's modulus, $G_{o,+}$ corresponds to a vessel with thicker (more rigid) walls at the center (more rigid), and $G_{o,-}$ denotes a vessel with walls that are less thick (less rigid) at the center of the vessel.

Let us take the Young's modulus to be $E_Y = 300$ k Pa. The corresponding wall thicknesses are $h_d = R_o/10$ for G_o, and $h_{d,\pm} = \frac{1}{10}R_o\left[1 \pm \frac{1}{2}\sin\left(\pi\frac{x-\frac{1}{2}}{4}\right)\right]$ for $G_{o,\pm}$. That is, for the non uniform parameters, the wall thickness may vary from 5 to 15% of the unstressed radius.

The right panel of Figure 10 shows a profile of the different elasticity parameter G_o. Furthermore, the initial conditions are

$$A(x, 0) = A_o(x) = 0.82 \text{ cm}, \quad u(x, 0) = 0, \ \ 0 \le x \le 5 \text{ m}. \tag{44}$$

As mentioned above, the velocity is prescribed at the left boundary by the time series shown in the left panel of Figure 10. Zero Neumann boundary conditions are applied to A at the left boundary and both A and Q at the right boundary.

The numerical solutions are shown in Figure 11 for G_o (black solid line), $G_{o,-}$ (red dotted line), and $G_{o,+}$ (blue dashed line). In each panel, we show the radius profiles for all elasticity parameters (left column) and the corresponding velocity profiles (right column). Section 4.3 in[4] provides estimates for the first time the shock wave forms, denoted by t_s. This is done for constant parameters and no source terms. Our elasticity parameters $G_{o,\pm}$ depend on x. Taking the minimum (20 k Pa), intermediate (40 k Pa), and maximum (60 k Pa) values, it provides times of $t_s = 0.34$ s, 0.48, and 0.59 s, respectively. In the first row, we see a similar behaviour in all cases, with an increment in the cross-sectional area and velocity due to the discharge coming from the left boundary. As the flow moves to the right, the fluid interacts with an artery that may have different elastic properties. At time $t = 0.48$ s, a shock wave has formed for the less-rigid-wall case ($G_{o,-}$), the artery with uniform elasticity (G_o) is getting close to forming a shock wave, while the more-rigid wall ($G_{o,+}$) has not formed a shock wave yet. The last row shows the later time $t = 0.59$ s, where the dotted red and solid black lines show well formed shock waves. We note that in all cases, the solution to the right of the shock waves is flat due to the well-balanced property and the zero-Neumann boundary conditions. The amplitude of the radius perturbation is smaller but propagates faster compared to the other two cases. In the case of artery with less rigid walls towards the center ($G_{0,-}$), a shock wave forms earlier at time $t = 0.48$ s. One can conclude that for the parameters values used here, the profiles suggest that more elastic vessels are more susceptible to shock formation. In[4], it was observed that including vessel tapering, consisting of a linearly decreasing unstressed area A_o as a function of x delays the formation of shock waves.

4.5 | Cardiac cycle in tilted vessel

The effects of gravity are relevant in tilted or vertical arteries. Here, we also consider an artery pointing down with angle

$$\theta(s) = -\frac{\pi}{4}\frac{s}{5 \text{ m}}, 0 \le s \le 5 \text{ m}.$$

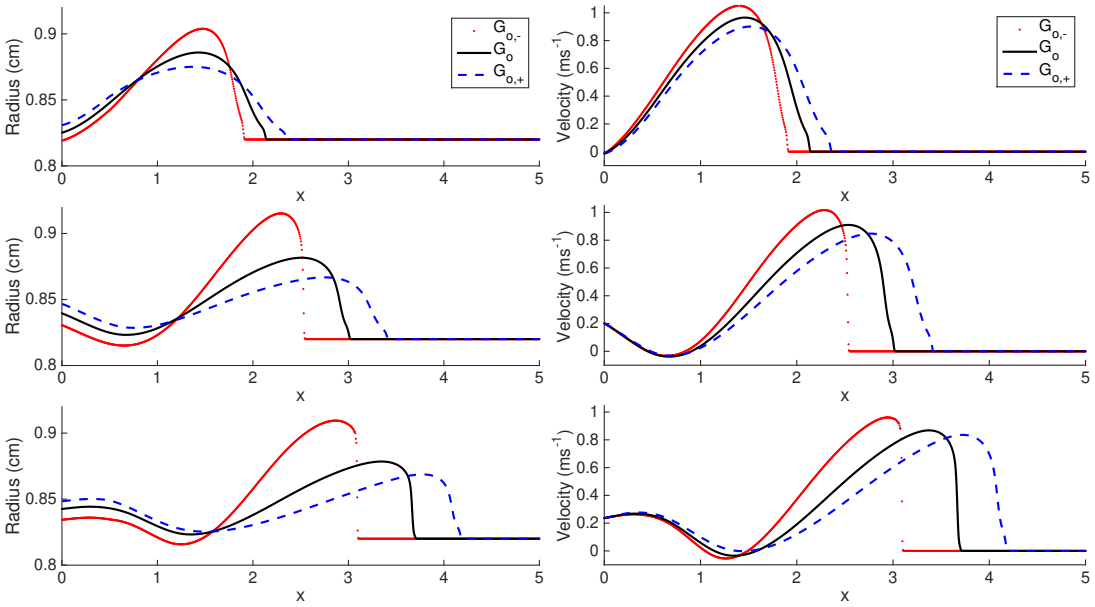

FIGURE 11 Radius (left) and velocity (right) profiles at times $t = 0.34$ s (top), $t = 0.48$ s (middle), and $t = 0.59$ s (bottom) obtained with elastic parameters G_o (black solid line), $G_{o,+}$ (blue dashed line), and $G_{o,-}$ (red dotted line). The initial conditions are given by (44).

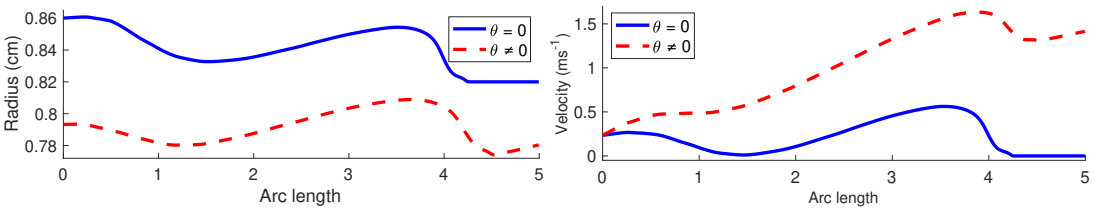

FIGURE 12 . Radius (left) and velocity (right) profiles at time $t = 0.6$ s. Here, $G_o = 40$ k Pa is constant, and the angle of the artery with respect to the horizontal axis is $\theta(s) = -\frac{\pi}{4}\frac{s}{5\,\mathrm{m}}$ (dashed red line). For comparison, we include the horizontal case $\theta = 0$ (solid blue line). The initial conditions are given by (44), and the same upstream boundary conditions used in the previous numerical test are implemented.

In this scenario, gravity accelerates the flow and the fluid leaves the domain through the right boundary. Figure 12 shows the radius (left) and velocity (right) as functions of s at time $t = 0.6$ s (red dashed lines). The blue solid lines correspond to the simulation of a horizontal artery with $\theta = 0$, which we show here for comparison. As expected, the fluid in the tilted vessel travels faster and reaches the right boundary, leaving the domain and reducing the cross sectional area. The maximum velocity in the tilted artery is 1.6 ms^{-1}, which is approximately three times larger than the maximum velocity in the horizontal artery (0.56 ms^{-1}).

4.6 | Tapered aorta

In[21], a comparison of computational hemodynamics in arteries between a 1D and a 3D formulation is presented. It was concluded that the 1D model gives a reasonable approximation of the global behavior of the spatially averaged pressure and flow waveforms. Blood flows through the aorta was simulated. The pressure over time was computed at given locations to compare 1D and 3D models. Here, we simulate blood passing through the full aorta, but we ignore the branches. The arc length domain is $[s_o, s_1]$,

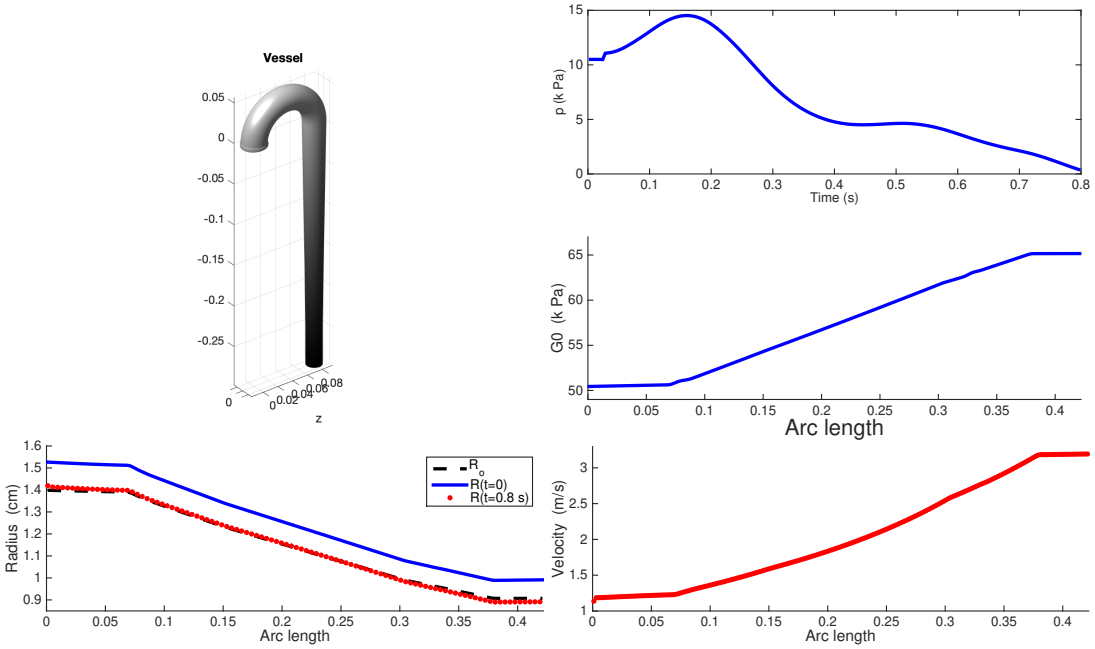

FIGURE 13 Blood flow simulation passing through the full aorta. Top left: 3D view of the axi-symmetric tapered vessel. Middle right: Profile of G_o. Bottom left: Profile of R_o (black dashed line), the initial radius (solid blue line), and the radius at time $t = 0.8$ s (dotted red line). Top right: Pressure measured at the middle of vessel ($s = 21.105$ cm) as a function of time. Bottom right: Velocity as a function of arc length at time $t = 0.8$ s.

where $s_o = 0, s_1 = 42.21$ cm. As an approximation to the aorta's curvature, the angle $\theta(s)$ is given by

$$\theta(s) = \frac{\pi}{2}\left[1 - 2\min\left(\frac{s}{0.3s_1}, 1\right)\right]. \tag{45}$$

That is, the vessel is straight up at the upstream boundary ($\theta = \pi/2$) and points down ($\theta = -\pi/2$) at position $s = 12.67$ cm.

We take this as an approximation to obtain the curvature of the full aorta. The parameter R_o is piecewise linear according to the radius at diastolic pressure shown in table IV in[21]. The values are written in Table 1. This determines the geometry of the vessel. The parameter G_o is given by equation (3) with $r_d = R_o$, and $h_d = r_d/10$. The pulse wave speed is a piecewise linear function according to the values provided in table IV in[21]. The graph for G_o is given in the middle right panel of Figure 13. The graph of A_o is given in the bottom left panel.

Here, the viscosity parameter is $\nu = 2.6 \times 10^{-6}$ m^2 s^{-1}. The initial conditions correspond to steady states at rest in a tilted vessel. That is, $u = 0$ and the cross sectional area satisfies equation (7), or equivalently,

$$A = A_o(s)\left(1 + \frac{p_o - g\rho z(s)}{G_o(s)}\right)^{2/\beta},$$

where $p_o = 20$k Pa and $\beta = 2$. The value of p_o was chosen so that the initial cross-sectional area is greater than the parameter A_o. See bottom left panel of Figure 13.

At the left boundary, we impose the velocity given by the profile in Figure 10 and Dirichlet boundary conditions for the cross-sectional area $A = A_o$. The discharge at the left boundary breaks the balance and induces a moving state. Neumann boundary conditions are imposed at the right boundary.

Figure 13 (top left panel) shows a 3D view of the axi-symmetric tapered vessel at time $t = 0.8$ s. Here, we use 200 grid points. The radius as a function of arc-length is also shown in the bottom left panel (red dotted line). The vessel's radius at the end time is closer to R_o, suggesting that the potential energy in Proposition 6 is dominated by gz. The bottom right panel shows the velocity as a function of time at $t = 0.8$ s. The discharge at the left boundary and the gravity generate a positive increasing velocity as a function of arc length. The top right panel shows the pressure measured at the middle of the vessel ($s = 21.105$ cm) as a function of time. The pressure reaches its maximum of approximately 14.52 k Pa at approximately $t = 0.1$ s, followed by

Segment	Length (cm)	Left radius (cm)	Right radius
I	7.0357	1.52	1.39
II	0.8	1.39	1.37
III	0.9	1.37	1.35
IV	6.4737	1.35	1.23
V	15.2	1.23	0.99
VI	1.8	0.99	0.97
VII	.7	0.97	0.962
VIII	.7	0.962	0.955
IX	4.3	0.955	0.907
X	4.3	0.907	0.86

TABLE 1 Aorta's geometry and dimensions.

a decay. Our theoretical and numerical setups are not identical to those in [21]. For instance, we do not include any of the aorta's branches, and we only use an approximated curvature where the effects of gravity are taken into consideration. Despite all the differences, the profiles of pressure as a function of time are qualitatively similar.

5 | CONCLUSIONS

It has been documented in the literature that 1D blood flow models may be a reasonable approximation as compared to their 3D counterparts. The 1D model analyzed here was described by a hyperbolic balance law. A key step for a good approximation is the accurate numerical computation of the 1D model. To that end, the hyperbolic properties of the system were described. For instance, a distinguished attribute of this model is that its source terms do not involve derivatives of the unknown solution. That is, the model does not have non-conservative products. The absence of non-conservative products avoids both theoretical and numerical complications. On the other hand, the characterization of steady-state flows was provided, even in the presence of viscosity. As stated in Corollary 1, a novel invariant quantity was found for moving states at equilibrium (non-vanishing velocity) in horizontal vessels. It was also shown that the model has an associated entropy function when the flow is inviscid and $\alpha = 1$. This is an important property, which can help in choosing physically relevant weak solutions.

All of the above features are good properties that can help construct robust, stable, and accurate numerical schemes to approximate solutions. At a discrete level, the numerical scheme may inherit some of the model's properties at the continuous level. For instance, a large class of semi-discrete entropy-satisfying numerical schemes was described. A well-balanced positivity-preserving central-upwind scheme is constructed, and its properties were proved via different propositions.

Several numerical tests were conducted to show the merits of the numerical scheme. The first three numerical tests helped us show that the numerical scheme is robust, stable and accurate. However, the ultimate goal of this work was the application of the model to more relevant situations from the medical point of view. One such application was conducted to analyze the effect of heterogenous elastic properties in the formation of shock waves. For the values of the parameters considered here, it was found that as the rigidity of the walls increases, the formation of shock waves is delayed. We also measured the gravity effect in a tilted vessel. We analyzed the velocities and radii both for horizontal and tilted vessels with negative angles. A smaller radius and higher velocity were revealed due to gravity. Ignoring bifurcations, the last numerical test considered a fluid passing through the tapered aorta. Once the model parameters and boundary conditions were specified, the solution was computed at $t = 0.8$ s and provided interesting results. The velocity increases with respect to arc length. The positive discharge at the left boundary and effect of gravity near the right boundary are consistent with the increasing velocity. The pressure at $s = 21.105$ cm was plotted as a function of time. The pressure reaches its maximum, followed by a decay. The profile is qualitatively similar to those found in other studies.

The 1D approach to simulate blood flows has been shown to be useful in different scenarios, such as in computing the propagation of pressure waves. However, important limitations may exist. The cross-sectional area is assumed to be a disk. Bifurcations are not considered in this work. A realistic scenario may also require a much more complex geometry, which

will be considered in future work. Modellers interested in hemodynamics using simplified models may find it helpful to seek numerical applications in cases that are relevant from a medical point of view after testing their numerical schemes to guarantee stability, robustness and accuracy.

References

1. Taylor C, Figueroa C. Patient-Specific Modeling of Cardiovascular Mechanics. *Annual Review of Biomedical Engineering* 2009; 11(1): 109-134. PMID: 19400706doi: 10.1146/annurev.bioeng.10.061807.160521

2. Quarteroni A, Manzoni A, Vergara C. The cardiovascular system: Mathematical modelling, numerical algorithms and clinical applications. *Acta Numerica* 2017; 26: 365?590. doi: 10.1017/S0962492917000046

3. Čanić S. Blood flow through compliant vessels after endovascular repair: wall deformations induced by the discontinuous wall properties. *Computing and Visualization in Science* 2002; 4(3): 147–155. doi: 10.1007/s007910100066

4. Čanić S, Kim EH. Mathematical analysis of the quasilinear effects in a hyperbolic model blood flow through compliant axi-symmetric vessels. *Mathematical Methods in the Applied Sciences* 2003; 26(14): 1161–1186. doi: 10.1002/mma.407

5. Čanić S, Hartley CJ, Rosenstrauch D, Tambača J, Guidoboni G, Mikelić A. Blood flow in compliant arteries: an effective viscoelastic reduced model, numerics, and experimental validation. *Annals of Biomedical Engineering* 2006; 34(4): 575–592.

6. Čanić S, Galovic M, Ljulj M, Tambaca J. A Dimension-Reduction Based Coupled Model of Mesh-Reinforced Shells. *SIAM Journal on Applied Mathematics* 2017; 77(2): 744–769.

7. Ku DN, Giddens DP, Zarins CK, Glagov S. Pulsatile flow and atherosclerosis in the human carotid bifurcation. Positive correlation between plaque location and low oscillating shear stress. *Arteriosclerosis, thrombosis, and vascular biology* 1985; 5(3): 293–302.

8. Formaggia L, Nobile F, Quarteroni A, Veneziani A, Zunino P. Advances on numerical modelling of blood flow problems. In: ; 2000: 11–14.

9. Quarteroni A, Formaggia L. Mathematical modelling and numerical simulation of the cardiovascular system. *Handbook of numerical analysis* 2004; 12: 3–127.

10. Müller LO, Parés C, Toro EF. Well-balanced high-order numerical schemes for one-dimensional blood flow in vessels with varying mechanical properties. *Journal of Computational Physics* 2013; 242: 53 - 85. doi: https://doi.org/10.1016/j.jcp.2013.01.050

11. Gino I. Montecinos EFT. Hyperbolic reformulation of a 1D viscoelastic blood flow model and ADER finite volume schemes. *Journal of Computational Physics* 2014; 266: 101-123.

12. LO Müller PB. Consistent treatment of viscoelastic effects at junctions in one-dimensional blood flow models. *Journal of Computational Physics* 2016; 314: 167-193.

13. Grinberg L, Cheever E, Anor T, Madsen JR, Karniadakis GE. Modeling Blood Flow Circulation in Intracranial Arterial Networks: A Comparative 3D/1D Simulation Study. *Annals of Biomedical Engineering* 2011; 39(1): 297–309. doi: 10.1007/s10439-010-0132-1

14. Nan Xiao JACAF. A systematic comparison between 1-D and 3-D hemodynamics in compliant arterial models. *International Journal for Numerical Methods in Biomedical Engineering* 2014; 30(2): 204-231.

15. Huges TJR, Lubliner J. On the One-Dimensional Theory of Blood Flow in the Larger Vessels. *Mathematical Biosciences* 1973; 18: 161-170.

16. Formaggia L, Lamponi D, Quarteroni A. One-dimensional models for blood flow in arteries. *Journal of Engineering Mathematics* 2003; 47(3): 251–276. doi: 10.1023/B:ENGI.0000007980.01347.29

17. Willemet M, Alastruey J. Arterial Pressure and Flow Wave Analysis Using Time-Domain 1-D Hemodynamics. *Annals of Biomedical Engineering* 2015; 43(1): 190–206. doi: 10.1007/s10439-014-1087-4

18. Ku DN. BLOOD FLOW IN ARTERIES. *Annual Review of Fluid Mechanics* 1997; 29(1): 399-434. doi: 10.1146/annurev.fluid.29.1.399

19. Vosse v. dFN, Stergiopulos N. Pulse Wave Propagation in the Arterial Tree. *Annual Review of Fluid Mechanics* 2011; 43(1): 467-499. doi: 10.1146/annurev-fluid-122109-160730

20. Huberts W, Van Canneyt K, Segers P, et al. Experimental validation of a pulse wave propagation model for predicting hemodynamics after vascular access surgery. *Journal of biomechanics* 2012; 45(9): 1684–1691.

21. Xiao N, Alastruey J, Alberto Figueroa C. A systematic comparison between 1-D and 3-D hemodynamics in compliant arterial models. *International journal for numerical methods in biomedical engineering* 2014; 30(2): 204–231.

22. Barnard A, Hunt W, Timlake W, Varley E. A theory of fluid flow in compliant tubes. *Biophysical journal* 1966; 6(6): 717–724.

23. Castro MJ, Pardo Milanés A, Parés C. Well-balanced numerical schemes based on a generalized hydrostatic reconstruction technique. *Mathematical Models & Methods in Applied Sciences* 2007; 17(12): 2055–2113. doi: 10.1142/S021820250700256X

24. Lucas O. Müller EFT. Well-balanced high-order solver for blood flow in networks of vessels with variable properties. *International Journal for Numerical Methods in Biomedical Engeneering* 2013; 29(12): 1388-1411.

25. LeVeque RJ. *Finite volume methods for hyperbolic problems*. Cambridge Texts in Applied MathematicsCambridge University Press, Cambridge . 2002

26. Toro EF. *Riemann solvers and numerical methods for fluid dynamics: A practical introduction*. Springer-Verlag, Berlin. third ed. 2009

27. Kurganov A, Tadmor E. New high-resolution central schemes for nonlinear conservation laws and convection-diffusion equations. *Journal of Computational Physics* 2000; 160(1): 241–282.

28. Kurganov A, Noelle S, Petrova G. Semidiscrete central-upwind schemes for hyperbolic conservation laws and Hamilton-Jacobi equations. *SIAM J. Sci. Comput.* 2001; 23(3): 707–740 (electronic). doi: 10.1137/S1064827500373413

29. Kurganov A, Tadmor E. Solution of two-dimensional Riemann problems for gas dynamics without Riemann problem solvers. *Numer. Methods Partial Differential Equations* 2002; 18(5): 584–608. doi: 10.1002/num.10025

30. Kurganov A, Lin CT. On the reduction of numerical dissipation in central-upwind schemes. *Commun. Comput. Phys.* 2007; 2(1): 141–163.

31. Beljadid A, Mohammadian A, Kurganov A. Well-balanced positivity preserving cell-vertex central-upwind scheme for shallow water flows. *Computers & Fluids* 2016; 136: 193–206.

32. Russo G. Central schemes for balance laws. In: . 141 of *Internat. Ser. Numer. Math., 140*. Basel: Birkhäuser. 2001 (pp. 821–829).

33. Vuković S, Sopta L. High-order ENO and WENO schemes with flux gradient and source term balancing. In: Kluwer/Plenum, New York. 2003 (pp. 333–346).

34. Geers A, Larrabide I, Morales H, Frangi A. Comparison of steady-state and transient blood flow simulations of intracranial aneurysms. In: ; 2010: 2622–2625.

35. Mynard J, Nithiarasu P. A 1D arterial blood flow model incorporating ventricular pressure, aortic valve and regional coronary flow using the locally conservative Galerkin (LCG) method. *Communications in Numerical Methods in Engineering* 2008; 24(5): 367–417.

36. Alastruey J, Parker KH, Sherwin SJ, others . Arterial pulse wave haemodynamics. In: Virtual PiE Led t/a BHR Group Lisbon, Portugal. ; 2012: 401–442.

37. Bessonov N, Sequeira A, Simakov S, Vassilevskii Y, Volpert V. Methods of blood flow modelling. *Mathematical modelling of natural phenomena* 2016; 11(1): 1–25.

38. Jung J, Lyczkowski RW, Panchal CB, Hassanein A. Multiphase hemodynamic simulation of pulsatile flow in a coronary artery. *Journal of biomechanics* 2006; 39(11): 2064–2073.

39. Dal Maso G, Lefloch PG, Murat F. Definition and weak stability of nonconservative products. *J. Math. Pures Appl. (9)* 1995; 74(6): 483–548.

40. LeFloch PG. *Hyperbolic systems of conservation laws*. Lectures in Mathematics ETH ZürichBirkhäuser Verlag, Basel . 2002. The theory of classical and nonclassical shock waves

41. LeFloch PG. Graph solutions of nonlinear hyperbolic systems. *J. Hyperbolic Differ. Equ.* 2004; 1(4): 643–689. doi: 10.1142/S0219891604000287

42. Abgrall R, Karni S. A comment on the computation of non-conservative products. *J. Comput. Phys.* 2010; 229(8): 2759–2763. doi: 10.1016/j.jcp.2009.12.015

43. Oleinik OA. Discontinuous solutions of non-linear differential equations. *Uspekhi Matematicheskikh Nauk* 1957; 12(3): 3–73.

44. Audusse E, Bouchut F, Bristeau MO, Klein R, Perthame B. A fast and stable well-balanced scheme with hydrostatic reconstruction for shallow water flows. *SIAM Journal on Scientific Computing* 2004; 25(6): 2050–2065 (electronic). doi: 10.1137/S1064827503431090

45. Bouchut F. *Nonlinear stability of finite volume methods for hyperbolic conservation laws and well-balanced schemes for sources*. Frontiers in MathematicsBasel: Birkhäuser Verlag . 2004.

46. Bouchut F, Luna M. dT. An entropy satisfying scheme for two-layer shallow water equations with uncoupled treatment. *ESAIM: Mathematical Modelling and Numerical Analysis* 2008; 42(4): 683 - 698. doi: 10.1051/m2an:2008019

47. Harten A, Lax PD, Leer vB. On upstream differencing and Godunov-type schemes for hyperbolic conservation laws. *SIAM Rev.* 1983; 25(1): 35–61. doi: 10.1137/1025002

48. Kurganov A, Levy D. Central-upwind schemes for the Saint-Venant system. *M2AN. Mathematical Modelling and Numerical Analysis* 2002; 36(3): 397–425. doi: 10.1051/m2an:2002019

49. Kurganov A, Petrova G. A second-order well-balanced positivity preserving central-upwind scheme for the Saint-Venant system. *Commun. Math. Sci.* 2007; 5(1): 133–160.

50. Balbás J, Karni S. A central scheme for shallow water flows along channels with irregular geometry. *M2AN. Mathematical Modelling and Numerical Analysis* 2009; 43(2): 333–351. doi: 10.1051/m2an:2008050

51. Chertock A, Cui S, Kurganov A, Wu T. Well-balanced positivity preserving central-upwind scheme for the shallow water system with friction terms. *International Journal for numerical methods in fluids* 2015; 78(6): 355–383.

52. Leer vB. Towards the ultimate conservative difference scheme. V. A second-order sequel to Godunov's method [J. Comput. Phys. **32** (1979), no. 1, 101–136]. *Journal of Computational Physics* 1997; 135(2): 227–248.

53. Jin S. A steady-state capturing method for hyperbolic systems with geometrical source terms. *M2AN. Mathematical Modelling and Numerical Analysis* 2001; 35(4): 631–645. doi: 10.1051/m2an:2001130

54. LeVeque RJ. Balancing source terms and flux gradients in high-resolution Godunov methods: the quasi-steady wave-propagation algorithm. *Journal of Computational Physics* 1998; 146(1): 346–365.

55. Vázquez-Cendón ME. Improved treatment of source terms in upwind schemes for the shallow water equations in channels with irregular geometry. *Journal of Computational Physics* 1999; 148(2): 497–526. doi: 10.1006/jcph.1998.6127

56. Gottlieb S, Shu CW, Tadmor E. Strong stability-preserving high-order time discretization methods. *SIAM Rev.* 2001; 43(1): 89–112 (electronic). doi: 10.1137/S003614450036757X

57. Andrianov N, Warnecke G. The Riemann problem for the Baer–Nunziato two-phase flow model. *Journal of Computational Physics* 2004; 195(2): 434–464.

58. Eckmann DM, Bowers S, Stecker M, Cheung AT. Hematocrit, volume expander, temperature, and shear rate effects on blood viscosity. *Anesthesia & Analgesia* 2000; 91(3): 539–545.

59. Rodero C, Conejero JA, García-Fernández I. Shock wave formation in compliant arteries. *Evolution Equations & Control Theory* 2019; 8(1): 221.